Superlattices and Microstructures, Vol. 29, No. 2, 2001
doi:10.1006/spmi.2000.0973
Available online at http://www.idealibrary.com on IDEAL®

Strong wavevector dependence of hole transport in heterostructures

GERHARD KLIMECK, R. CHRIS BOWEN
Jet Propulsion Laboratory, California Institute of Technology, Pasadena, CA 91109, U.S.A.

TIMOTHY B. BOYKIN
Department of Electrical and Computer Engineering and LICOS, The University of Alabama in Huntsville, Huntsville, AL 35899, U.S.A.

(Received 17 November 2000)

Heterostructures such as resonant tunneling diodes, quantum well photodetectors and lasers, and cascade lasers break the symmetry of the crystalline lattice. Such break in lattice symmetry causes a strong interaction of heavy-, light- and split-off hole bands. A resonant tunneling diode is used as a vehicle to study hole transport in heterostructures including the subband dispersion transverse to the main transport direction. Four key findings are demonstrated: (1) the heavy and light hole interaction is shown to be strong enough to result in dominant current flow off the Γ zone center (more holes flow through the structure at an angle than straight through), (2) explicit inclusion of the transverse momentum in the current integration is needed, (3) most of the current flow is due to injection from heavy holes in the emitter, and (4) the dependence on the angle ϕ of the transverse momentum $\boldsymbol{k}$ is weak. Two bandstructure models are utilized to demonstrate the underlying physics: (1) independent/uncoupled heavy-, light- and split-off bands, and (2) second-nearest neighbor sp3s* tight-binding model. Current–voltage (I–V) simulations including explicit integration of the total energy E, transverse momentum $|\boldsymbol{k}|$ and transverse momentum angle ϕ are analyzed. An analytic formula for the current density $J(k)$ as a function of transverse momentum k is derived and utilized to explain the three independent mechanisms that generate off-zone-center current flow: (1) nonmonotonic (electron-like) hole dispersion, (2) different quantum well and emitter effective masses, and (3) momentum-dependent quantum well coupling strength. The analytic expression is also used to generate a complete I–V characteristic that compares well to the full numerical solution. The Fermi level and temperature dependence on the I–V is examined. Finally a simulation is compared to experimental data.

© 2001 Academic Press

Key words: resonant tunneling, holes, anisotropy, transport.

1. Introduction

1.1. Nanoelectronic modeling (NEMO)

While silicon device technology dominates the commercial microprocessor and memory market, semiconductor heterostructure devices maintain their niche for light detection, light emission, and high-speed data

0749–6036/01/030187 + 30 $35.00/0 © 2001 Academic Press

transmission. Material variations on an atomic scale enable the quantum mechanical functionality of devices such as resonant tunneling diodes (RTDs), quantum well infrared photodetectors, quantum well lasers, and heterostructure field effect transistors. The production of these heterostructure devices is enabled by the advancement of material growth techniques, which opened a vast design space of material compositions, layer thicknesses and doping profiles. The full experimental exploration of this design space is unfeasible and a reliable design tool is needed.

The need for a device modeling tool has prompted a device modeling project at the Central Research Laboratory of Texas Instruments (which transferred to Raytheon Systems in 1997). NEMO was developed as a general-purpose quantum mechanics-based 1D device design and analysis tool from 1993–97. The tool is available to US researchers by request on the NEMO web site [1]. NEMO is based on the nonequilibrium Green function approach, which allows a fundamentally sound inclusion of the required physics: bandstructure, scattering, and charge self-consistency. The theoretical approach is documented in Refs [2, 3] while some of the major simulation results are documented in Refs [4–10]. NEMO development is presently continued at the Jet Propulsion Laboratory towards the modeling of light detection and emission devices.

The work presented here was enabled by the implementation of parallelism in NEMO on simultaneous, various levels: voltage, transverse momentum integration and energy integration. The use of massively parallel computers enabled the thorough exploration of the state space in total energy E and transverse momentum k for a significant number of bias points.

1.2. Why quantum mechanical hole transport?

In most high-speed quantum devices an attempt is made to utilize the high electron mobility in III–V materials. Quantum mechanical carrier transport research has, therefore, focused on pure electron transport. Optical devices, however, typically involve quantum states in the valence bands. To begin the study of quantum mechanical electron and hole transport in laser structures using NEMO the pure hole transport in a hole-doped RTD is examined.

It is well known that hole transport is strongly influenced by coupling between the light hole (LH), heavy hole (HH) and split-off (SO) valence bands [11–14]. Band coupling occurs due to translational symmetry breaking inherent in any interesting electronic device. Valence bands in semiconductors are also intrinsically coupled via the spin–orbit interaction. Envelope function representations have been used extensively in much of the published work on hole transport [15–22]. This paper is an extension of previous work by Kiledjian *et al*. [23, 24] who use a nearest neighbor sp3s* empirical tight-binding basis which includes the spin–orbit interaction to all orders and incorporates wavefunction coupling at interfaces through orbital interactions. To better fit the complicated valence band dispersion we include both nearest and second-nearest neighbor interactions [25]. Subband energies and widths are calculated [26] as a function of transverse momentum allowing for a detailed and intuitive analysis of hole transport mechanisms.

1.3. Overview of the paper

Sections 2 and 3 discuss approximations for calculating current density and details our approach for explicitly including its dependence on transverse momentum. Section 4 is a brief review of the complexities involved in quantum transport through valence band derived states. The density of states is used to identify the symmetry and number of nodes of the confined states and it is related to the transmission coefficients. Hole anisotropy and its effect on quantum well subbands is discussed. The complicated subband structure results in a strong dependence of transmission characteristics as a function of transverse momentum. Section 5 details features in current density versus total energy and transverse momentum for a simple RTD structure. Failure of the Esaki–Tsu approximation and significant current contributions off-zone-center are shown. In Section 6, an analytic expression for current density as a function of transverse momentum is derived and used to better understand the numerical results of Section 5. Sections 7 and 8 discusses the emitter Fermi level and temperature dependence of hole transport, respectively. In Section 9 we test the validity of the axial symmetry approximation by calculating the dependence of the current density on the axial incidence angle. A comparison between theory and experiment is examined in Section 10. Detailed discussions on the bias dependence of the resonance energies and widths are deferred to Appendices A and B, respectively. Appendix C tabulates the sp3s* second-nearest neighbor parameters used in this work and lists the associated material parameters such as bandgaps and effective masses.

2. The central quantity: current density $J(k)$

Typical high-performance RTDs used for memory [27] and logic [28] devices are based on electron (rather than hole) transport in direct gap material systems. Electron states are occupied close to the Γ point and the bands can typically be assumed to be isotropic.[†] For high current density devices operated at room temperature the effects of incoherent scattering inside the central RTD region [5, 8–10] have been shown to be negligible while bandstructure effects such an nonparabolicity and complex band wrapping are dominant [5–7]. In such a case the current can be computed [2, 7] using an expression of the form

$$J \propto \int dE \int d\phi \int kdkT(E,k,\phi)\,(f_L(E) - f_R(E)) \tag{1}$$

$$\propto \int dE \int kdkT(E,k)\,(f_L(E) - f_R(E)) \tag{2}$$

$$= \int dE \int kdkJ(E,k) \tag{3}$$

where k is the electron momentum transverse to the transport direction normalized to the unit cell a by $\frac{\pi}{a}$, ϕ is the momentum angle, E is the total energy, T is the transmission coefficient, and $f_{L/R}$ is the Fermi function in the left/right contact. A discussion of the dependence of the transmission coefficient on ϕ is deferred to Section 9 and for now it is assumed that the transmission coefficient is independent of ϕ.

The transmission coefficient $T(E,k)$ may be expensive to compute, since it may contain sharp resonances (10^{-9}–10^{-3} eV) that have to be resolved well in an energy range of typically 1 eV. During the NEMO project algorithms that locate [26] and resolve [29] the resonances expedite the computation of $T(E, k = \text{const})$. It is therefore convenient for numerical reasons to reverse the order of integration in eqn (3) and to define an intermediate quantity $J(k)$ as follows:

$$J(k) = \int dE\,J(E,k) \tag{4}$$

such that

$$J \propto \int kdkJ(k). \tag{5}$$

This quantity $J(k)$ is not only numerically convenient, but it also bears physical insight as to ‘where’ the carrier transport occurs in k-space. It will be shown analytically in Sections 6.1 and 6.2 that for an electron RTD the function $J(k)$ is peaked at $k = 0$ and monotonically decreases with k. This behavior indicates that the dominant current contribution arises from carriers at the Brillouin zone center Γ. For holes, however, it will be shown that $J(k)$ can exhibit sharply peaked features *outside* ($k > 0$) the Brillouin zone center Γ. This indicates that more holes traverse the structure at an angle than straight through the heterointerfaces. This is one of the central results of this paper.

[†] A typical barrier material in GaAs and InP substrate material systems is AlAs, which has an indirect bandgap. However, the contacts and the quantum well are typically direct bandgap materials.

3. Tsu–Esaki formula

One common approach in reducing the required CPU time needed to compute a complete I–V characteristic is the assumption of parabolic transverse subbands such that the transmission coefficient has an analytic, parabolic transverse momentum dependence: $T(E, k) = T(E - \hbar^2k^2/2m^*, k = 0)$. Under this assumption the transverse momentum integration in eqn (2) can be carried out analytically to result in the so-called Tsu–Esaki [30] formula:

$$J \propto \rho_{2D} \int dE\, T(E, k = 0) \ln\left(\frac{1 + e^{(E_F - E)/k\mathcal{T}}}{1 + e^{(E_F - E - qV)/k\mathcal{T}}}\right). \tag{6}$$

The Tsu–Esaki 1D integration formula is capable of providing qualitatively correct results for electron devices given the restrictive assumption that subband alignment is *not* the primary transport mechanism [7, 31–33]. Technologically relevant RTDs that show negative differential resistance at room temperature all exhibit a triangular emitter well such that there is a large 2D to 2D subband tunneling contribution from the emitter to the central resonance. To achieve quantitative agreement [6, 7] between simulation and experimental data for such RTDs full 2D integrations in energy E and transverse momentum k according to eqn (3) must be performed. This paper will show in Section 6.3 an example of good agreement between the Tsu–Esaki approximation and the full band integration for a structure that has flat band conditions in the emitter and therefore provides a 3D emitter to 2D quantum well tunneling process. We emphasize here in advance that such a simulation is included for pedagogical reasons only, to show the simple behavior of $J(k)$ for electrons. The rest of the paper underlines that the analytical Tsu–Esaki integration over the transverse momentum becomes completely invalid for hole transport [23, 24].

4. Spectral quantities: density of states, transmission, and subbands

4.1. Independent, uncoupled single bands

The model RTD considered here consists of 10 monolayer (ml) AlAs barriers with a 20 ml GaAs well. To avoid complications due to triangular notch states outside the RTD a linear potential drop is applied.† A degenerate hole Fermi level of 8.4 meV is assumed corresponding to a doping of 10^{18} cm^{-3}.

The simplest approach to hole transport available in NEMO is the independent treatment of the LH and HH bands in a single-band tight-binding basis. Within the single-band model the effective masses and band offsets can be freely chosen. For the LH band simulation the following effective masses and valence band offset are used: $m_{\mathrm{GaAs}} = 0.071$, $m_{\mathrm{AlAs}} = 0.15$, and $\Delta E_v = -0.545$ eV. For the HH simulation the corresponding values $m_{\mathrm{GaAs}} = 0.41$, $m_{\mathrm{AlAs}} = 0.48$, and $\Delta E_v = -0.545$ eV are used. These masses correspond to values that our sp3s* second-nearest neighbor predicts in the [001] direction (see Table 1 in Appendix C).

Figure 1 shows the zero-bias density of states and transmission coefficients for the independent single-band models. The density of states shows the nodal structure of the central RTD resonances. Each of the resonances corresponds to a peak in the transmission curve. The LH density of states (Fig. 1A) and transmission coefficient (Fig. 1B) look similar to the density of states presented in Fig. 2 of Ref. [7]. The HH mass is significantly larger than the light mass resulting in a smaller energy separation between the confined states.‡The barriers are much more opaque for the heavy electrons than the light electrons resulting in much stronger confinement.§This stronger confinement reveals itself in a significantly larger intrinsic lifetime of the

---

† There is no implicit limitation in NEMO to a linear potential drop. Charge self-consistent simulations of the Hartree and exchange and correlation potential are presented in Refs [4, 6, 7].

‡ In an infinite barrier square well of width a the energy separation is $\Delta E_{n+1} = E_{n+1} - E_n \propto \hbar^2\pi^2/2ma^2 \propto 1/m$.

§ For a single square barrier of thickness d the exponential $e^{-\kappa d}$ decay constant is defined as $\kappa = \sqrt{2m\Delta E/\hbar^2} \propto \sqrt{m}$.

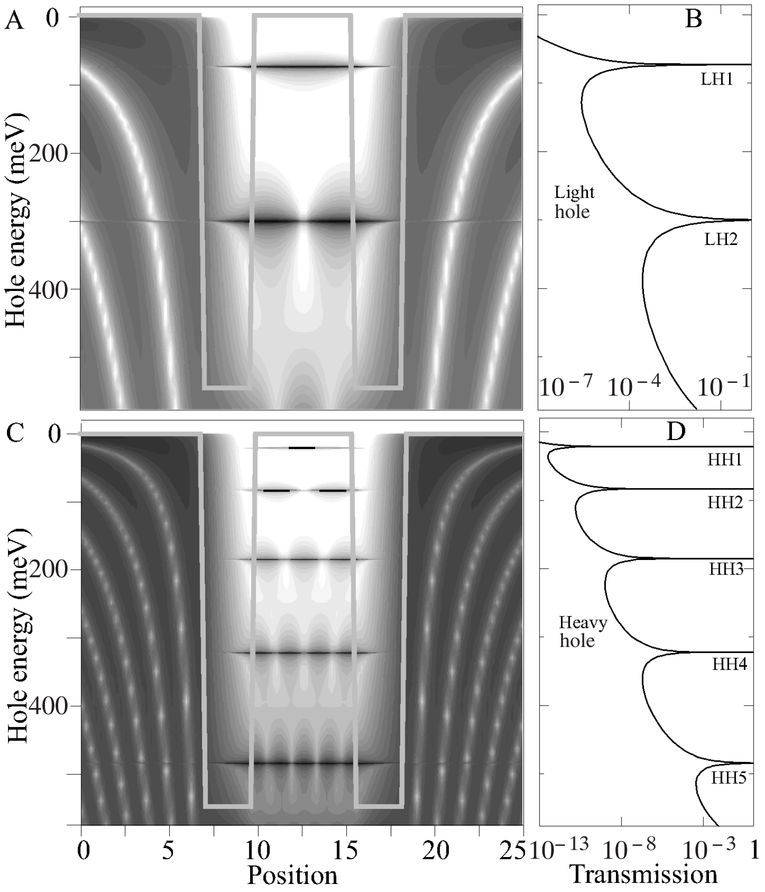

Fig. 1. Independent single-band density of states and transmission coefficients. A and B, LH; C and D, HH. On the gray scale dark (light) corresponds to high (low) density of states. Symmetries of the ground excited hole states are evident and aligned in energy with the transmission resonances. HH resonance are much narrower (resonance widths: 3.3×10^{-6}, 4.9×10^{-5}, 5.0×10^{-4}, 7.2×10^{-3}, and 2.3×10^{-1} meV) than LH resonances (resonances widths: 3.3×10^{-2} and 5.9×10^{-1} meV).

resonance state, or equivalently in a much smaller resonance width. Indeed the NEMO resonance finder [26] indicates that the LH ground state is four orders of magnitude wider than the HH ground state as indicated in the caption of Fig. 1.

4.2. Comparison of single-band and multiband transmission coefficients

The RTD heterointerfaces as well as applied and built-in potentials break the translational symmetry in the growth direction. This symmetry breaking and the spin–orbit interaction couples the LH, HH and SO bands. To properly model such coherently coupled bands the multiband tight-binding sp3s* model is employed.

Figure 2 compares the previously calculated independent single-band transmission coefficients of Fig. 1B and D to a transmission coefficient based on the second-nearest neighbor tight-binding model. The general features of the multiband transmission coefficient resemble the sum of the individual LH and HH bands at low energies with $E < 0.2$ eV. On closer inspection it becomes clear, however, that the resonances one would associate with HH states do not result in a unity transmission coefficient. While the LH resonance transmis-

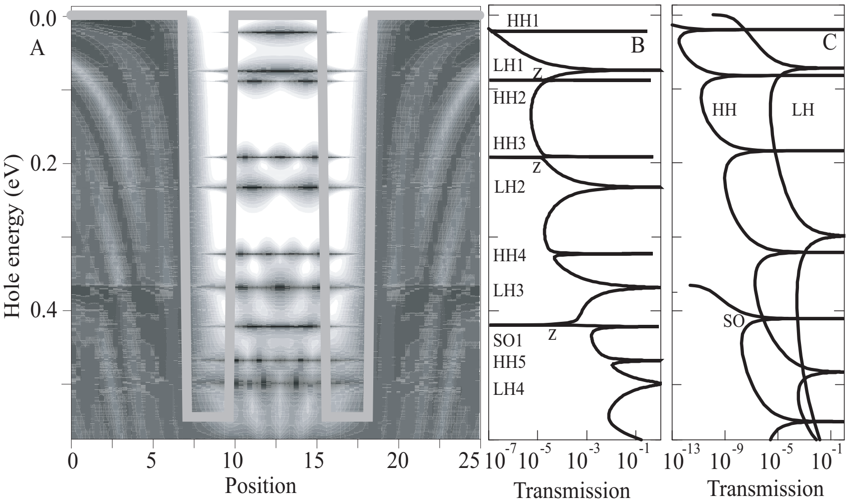

Fig. 2. Density of states A and transmission B computed in the sp3s* model. Resonance linewidths are HH1-5: 1.4×10^{-5}, 4.5×10^{-4}, 1.8×10^{-3}, 1.2×10^{-2}, 2.8×10^{0} meV, and LH1-4: 5.4×10^{-2}, 1.7×10^{0}, 4.6×10^{0}, 1.9×10 meV, and SO1 : 8.2×10^{-2} meV. Transmission zeros are labeled as z. C, Transmission coefficient in the independent single-band model from Fig. 1B and D, for the LH and HH effective mass model, as well as a single-band SO band model with $m_{\mathrm{GaAs}} = 0.14$, $E_{\mathrm{GaAs_{so}}} = -0.366$ eV, $m_{\mathrm{AlAs}} = 0.25$, and $E_{\mathrm{AlAs_{so}}} = -0.883$ eV.

sion looks close to (labeled as ‘z’ in Fig. 2B) one on the logarithmic scale it does not quite reach unity. Furthermore there are some transmission zeros evident in the multiband case [18, 20, 23]. These features are all characteristics of the Fano lineshape which occurs when a bound state is coupled to a continuum [34]. In the case of hole transport *all* the resonances are of the Fano type. Transmission zeros occur for isolated Fano resonances. The zeros move off the real axis in conjugate pairs for overlapped Fano resonances [26]. This explains the lack of transmission zeros for the LH resonances. Note that unlike the $k \cdot p$ model [20] the sp3s* model couples the LH, HH, and SO bands for $k = 0$ even for zero bias due to symmetry breaking and proper inclusion of the spin–orbit interaction.

The density of states in Fig. 2A shows the nodal symmetries of the LH, HH, and SO resonances. From the nodal symmetry one can identify the various LH, HH and SO resonances in the multiband transmission coefficient. Compared to the single-band results, the multiband LH resonances LH2 and LH3 move to lower hole energies. This can be explained by the strong LH band nonparabolicity that will be discussed in the next section in more detail. The HH2–4 states move slightly in the *opposite* direction which cannot be explained by band nonparabolicity. In Sections 6.4–6.6 and Appendix B we will show that these states are strongly coupled to the LH states as visible by strongly enhanced resonance linewidths. Such strong coupling corresponds to a lighter hole mass which causes the resonance energies to go up in energy more than states based on pure HH effective masses.

Note that the standing wave patterns outside the RTD of the de-coupled LH and HHs in Figs 1A and C are now washed out in Fig. 2. Only a weak standing wave pattern can be observed, indicating strong mixing of HH and LH states outside the RTD structure. For a larger picture of the typical standing wave pattern outside an RTD we refer the reader to Fig. 2 of Ref. [7]. A break in the standing wave pattern outside the RTD also shows the on-set of the SO band at about 0.366 eV.

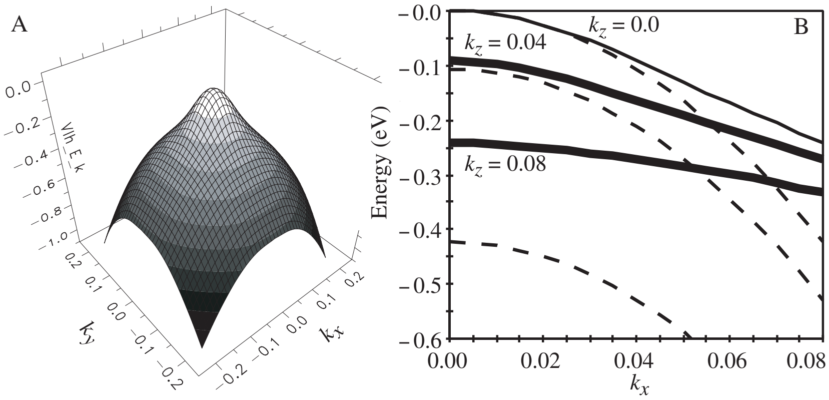

Fig. 3. A, LH dispersion surface in the [100] and [010] plane. B, Slices through the surface in A along k_x for three different momenta, $k_z = 0$, $k_z = 0.04$ and $k_z = 0.08$. $k_z = 0.04$, and $k_z = 0.08$ correspond to the first two quantized states in the model RTD presented here. Dashed curves indicate a perfectly parabolic, anisotropic dispersion computed with a LH mass of $m^* = 0.07$. Note the large discrepancy between the nonparabolic bands and the parabolic bands at larger k values. The energy and curvature of the first excited subband with $k_z = 0.08$ is modeled completely incorrectly using an anisotropic parabolic dispersion.

4.3. LH and HH anisotropy and their effects on the transverse subbands

The LH and HH bands in typical III–V semiconductors are anisotropic. Hole mass measurements are available [35] for a variety of material systems in the [100], [110], and [111] directions. Table 1 in Appendix C contains measured [35] HH, LH, and SO band masses and their values in our sp3s* second-nearest neighbor tight-binding models for the case of GaAs and AlAs. We use the second-nearest neighbor model since it has been shown [25, 36] that it offers a higher degree of freedom to independently adjust masses in the [100], [110] and [111] directions compared to the nearest neighbor tight-binding model.

We emphasize here that the overall results presented in this paper such as off-zone-center current flow and transverse momentum dependence are *not* unique to the second-nearest neighbor model. We have verified that they can be observed in the nearest neighbor sp3s* model as well. However, the hole anisotropy is not represented as well in the nearest neighbor model.

The introduction of a double barrier heterostructure causes a quantization of the crystal momentum in one (the growth/longitudinal) direction. In the transverse direction the plane wave crystal momentum remains a good quantum number and the dispersion is described by subbands. In this section the construction of these subbands including the effects of the LH and HH anisotropy is illustrated. To present the physical argument for the shape of the dispersion we start from a bulk band structure that includes the band anisotropy.

Figure 3A shows a surface plot of the LH bulk dispersion in the [100]/[010] plane computed with our second-nearest neighbor sp3s* model. Figure 3B shows three slices taken through the [010] axis plotted along [100] through the surface shown in A. If the LH band were perfectly parabolic, Fig. 3A would show an anisotropic paraboloid, and slices along this paraboloid would be perfect parabolas as indicated by the dashed curves in Fig. 3B.

The heterostructure growth quantizes states along the growth direction. Assume that $E_1 = E(k_1 \approx \pi/\Delta \approx 0.04)$ is the ground state energy† of the man-made resonator of length Δ. $E_2 = E(k_2 = 2k_1 \approx 0.08)$ and $E_3 = E(k_3 = 3k_1 \approx 0.12)$ are the first and second excited state energy, respectively. E_1 and E_2 are

---

[†] The resonator we consider in the numerical studies has a width of 20 atomic monolayers ($\Delta = 20a$) of GaAs which corresponds to a value of $k_1 \approx \frac{\pi/\Delta}{\pi/a} = \frac{\pi}{a} = 0.05$, where a is the atomic unit cell. However, the wavefunctions do penetrate into the barriers significantly and we get better agreement between the analytic dispersions and the numerical dispersions at $k_1 \approx 0.04$ which corresponds to a 25 ($\Delta = 25a$) monolayer well, or a penetration of the wavefunction in the barriers of 2.5 monolayers at each side.

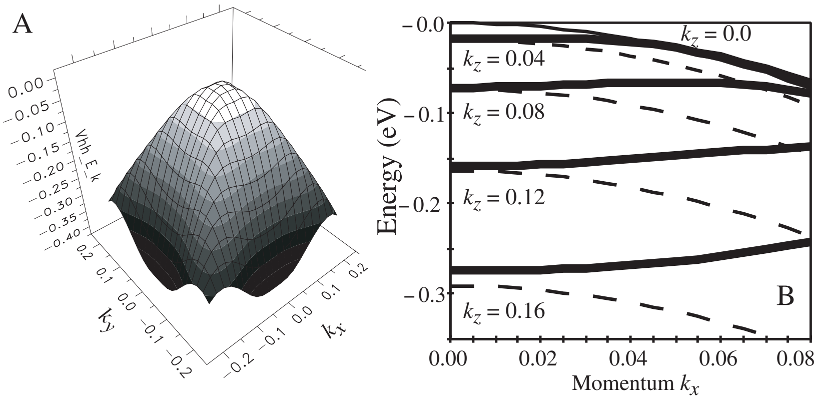

Fig. 4. A, HH dispersion surface in the [100] and [010] plane. The ridge in the [110] direction is evidence of the heavier mass in the [110] direction than the [100] direction. B, Slices through the surface in A along k_x for five different momenta, $k_z = 0$, $k_z = 0.04$, $k_z = 0.08$, $k_z = 0.12$, and $k_z = 0.16$. $k_z \neq 0.0$ correspond to the first quantized states in the model RTD presented here. Dashed curves indicate a perfectly parabolic, anisotropic dispersion computed with a HH mass of $m^* = 0.41$. Note the electron-like behavior compared to the perfect parabolic behavior.

depicted in Fig. 3B by heavy curves. The same figure shows perfect parabolic dispersions for E_1 and E_2 in dashed curves. The anisotropy of the LH band flattens out the transverse subband significantly, increasing the effective mass in the transverse direction. Movement down in energy of the LH2 and LH3 resonances was already seen in the comparison of transmission coefficients in Fig. 2B vs. C.

The transverse subband dispersion becomes more complex for the HH case. Figure 4A shows a surface plot of the HH dispersion in the [100]/[010] plane. The heavier mass in the [110] direction compared to the [100] direction clearly results in a ridge-like feature on the 2D surface. Figure 4B shows four slices taken through the [010] axis plotted along [100] through the surface shown in A. Again the dispersion is quantized by $k_1 \approx \pi/\Delta \approx 0.04$ as the ground state energy of the man-made resonator of length Δ. $k_2 = 2k_1$, $k_3 = 3k_1$, and $k_4 = 4k_1$ are the first, second, and third excited state respectively. In the case of HHs the anisotropy of the bands produces some unintuitive results: the excited HH states move *up* in energy rather than down in energy as the transverse momentum is increased [12, 37]. For comparison the dashed curves in the insert indicate a perfectly parabolic dispersion with the hole mass of $m^* = 0.41$. The electron-like behavior of the excited state subbands is clearly evident.

The next complication in the transverse subband dispersion is due to the coupling of the LH and HH bands due to the translational symmetry breaking. The transverse dispersion is computed for a hole GaAs/AlAs RTD consisting of 10 monolayer barriers and a 20 monolayer well. Figure 5 shows the plots of Fig. 3B and 4B overlayed compared to the RTD transverse subband dispersion. The coupling of the bands results in the mixing of LH and HH states and in anticrossings of the transverse subbands. This transverse subband dispersion shows a rich structure that is anything but parabolic. The question now arises to the effects of these nonparabolic subbands on the electron transport through the model RTD, which is the subject of the rest of this paper.

Note that the states in Fig. 2B are labeled in a sequence of HH1, LH1, HH2, HH3, LH2 according to their resonance linewidth and nodal feature size, while Fig. 5B reverses the order of LH1 and HH2 according to transverse momentum behavior. From the transverse dispersion in Fig. 5B it is clear that there is already an anticrossing of HH2 and LH1 at zero transverse momentum and these states are strongly interacting. From now on we will use the labeling in Fig. 5B according to the transverse momentum behavior and defer a more detailed discussion to Appendix B.

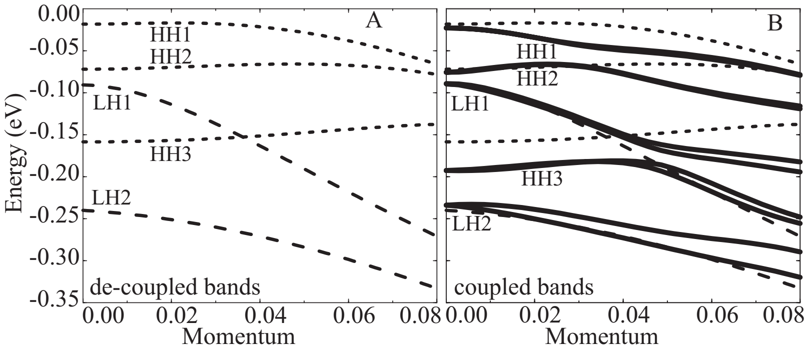

Fig. 5. A, Overlayed de-coupled LH (long dashed curves) and HH (short dashed curves) transverse dispersions from Figs 3B and 4B, respectively. B, Same as A combined with transverse dispersion computed in the sp3s* coupled band model in an open RTD system with 10 monolayer AlAs barriers and 20 monolayer GaAs quantum well (solid curve).

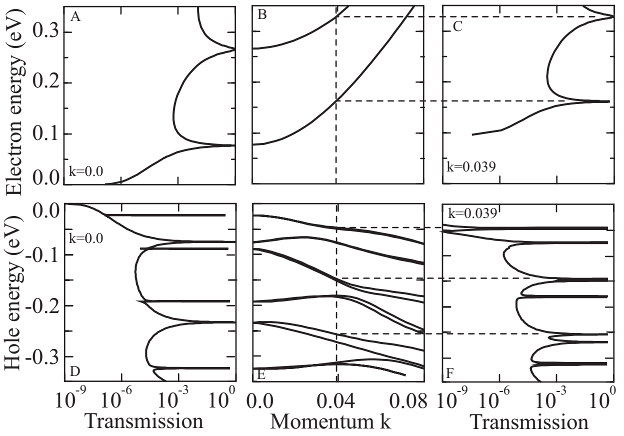

Fig. 6. A, B, and C refer to the GaAs/AlGaAs electron RTD described in the text; D, E, and F refer to the GaAs/AlAs hole RTD. No voltage is applied. A, Transmission coefficient $T(E, k = 0)$. B, Transverse electron subband. A small nonparabolicity is visible for the second state compared to the ground state. C, Transmission coefficient $T(E, k = 0.039)$. The curve is qualitatively identical to A except for the shift in energy. D, E, and F are the equivalents to A, B, and C for the hole RTD. The transmission coefficient in F is clearly not just an energy shifted version of the transmission coefficient of D. Spectral features have significantly shifted.

4.4. Transverse momentum-dependent transmission coefficients

Previous sections discussed the coupled HH and LH transmission coefficient for zero transverse momentum (Section 4.2) and the nontrivial HH and LH transverse subband dispersion (Section 4.3). This section combines these two aspects and demonstrates the strong momentum dependence of the transmission coefficients [24]. Figure 6 demonstrates this strong dependence by comparison to an electron RTD.

The electron RTD considered in this case is identical to the previously considered hole RTD except that the hole dopant is replaced by electron dopant and the AlAs barriers are replaced[†] by $\text{Al}_{0.4}\text{Ga}_{0.6}\text{As}$. Figure 6A shows the familiar transmission coefficient through an electron RTD at zero transverse momentum. Figure 6B shows the expected transverse dispersion for the ground and first excited state in a GaAs/AlGaAs RTD. Some nonparabolicity is evident in the first excited state. Figure 6C shows the transmission coefficient for a transverse momentum of $k = 0.039$. This transmission coefficient appears qualitatively to be just energy shifted from the one in Fig. 6A disregarding nonparabolicity in the second state. That is exactly the assumption that enters into the derivation of the Tsu–Esaki formula (eqn (6)). Note, however, that the transmission coefficient does *not* reach unity. We also refer back to our discussion on the validity of the approximation in Section 3.

[†] The use of AlAs barriers would introduce X states in the barriers which would clutter up the physical picture without further insight.

The lower three panels in Fig. 6 show the equivalent transmission coefficients and subband dispersion for the hole RTD. Unlike the electron case the transmission coefficient shown in Fig. 6F is not merely an energy shifted version of the zero transverse momentum case; in fact it has little resemblance at all. The energies and widths of the individual resonances are modified significantly. The resonance energies in Fig. 6F correspond to the dispersion in Fig. 6E with the dashed vertical line at $k = 0.039$. The spin splitting[†] in the dispersion of Fig. 6E results in double peaks of the transmission coefficient.

The strong transverse momentum dependence on the transmission coefficient shown in Fig. 6F will result in an interesting dependence of the current flow distribution in momentum and energy as discussed in the next section. A comparison between the momentum dependence of the electron and hole current flow based on their different dispersions can also be found in Ref. [38].

We have also examined the density of states and the structure of the eigenstates at $k = 0.039$ corresponding to Fig. 6F and found that the nodal symmetries that are visible in the density of states shown in Fig. 2 are completely broken. We expect this break in the symmetry to have significant effects on the strength of optical matrix elements and leave further discussion to a later publication.

5. Current densities

The previous section showed a rich structure in the transverse hole dispersion and transmission coefficients. In this section the transmission coefficient $T(E,k)$ is converted into a current density $J(E,k)$ and interesting physical features due to this structure are discussed in the context of: (1) features in the total energy E integration, (2) features in the momentum-dependent current density $J(k)$, and finally (3) features in the I–V characteristic.

5.1. Transverse momentum-dependent current carrying channels

Figure 7 demonstrates how the momentum dependence distributes the current flow through the hole RTD over various different energies in the case of a carrier temperature of 300 K. Panels A and C of Fig. 7 show the current density $J(E,k) = T(E,k)(f_L(E) - f_R(E))$ for two different transverse momenta at a small applied voltage of 0.011 V. Except for a small modification due the applied bias and the exponential energy modulation by the Fermi function (see the dashed curves indicating the Fermi functions as 4.2, 77, and 300 K) the current densities shown in Fig. 7A and C resemble the transmission coefficients in Fig. 6D and F well.

Figure 7B and D shows the running integrals ($\tilde{J}(E,k) = \int_{-\infty}^{E} dE' J(E',k)$) as a function of energy E corresponding to Fig. 7A and C. The running integral provides a simple way to analyze the importance of the various energy channels through the structure. Channels/resonances that carry significant current will contribute significantly to the running integral. While the zero transverse momentum case shows only one significant energy channel (single-step function) the nonzero transverse momentum case shows three different significant channels. Figure 7B and D show that the spectrum of transverse hole channels is changed

---

[†] The asymmetry of the applied bias has split the two spin states. Note that there is no magnetic field selection in these simulations. The spin degenerate states at $k = 0$ are split due to the translational symmetry breaking at $k > 0$. We use the notation ↑, ↓ as a shorthand to identify the two states. Since there is no selecting magnetic field we assume that, for example, LH1 ↑ actually consists of a linear combination of up and down spins.

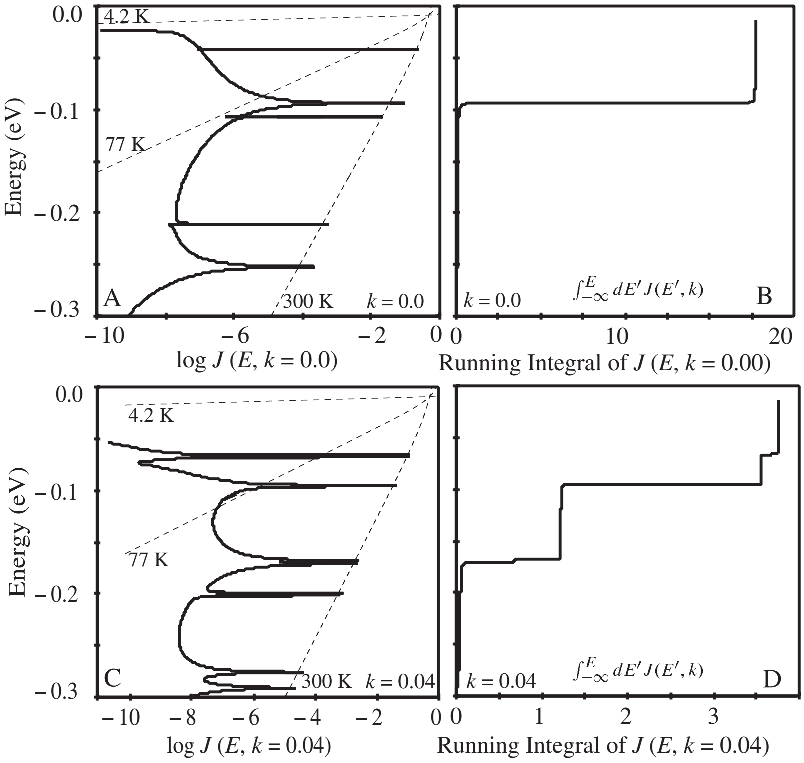

Fig. 7. A, Current density $J(E, k)$ for $k = 0$ as a function of energy E at a bias of 0.011 V and a temperature of 300 K on a log scale in arbitrary units. Dashed lines indicate Fermi functions at 4.2, 77, and 300 K. B, Running energy integral of A on a *linear* scale in arbitrary units. The major current contribution is occurring at one energy as indicated by the step. C, Same as A at a transverse momentum $k = 0.04$. Note that the curve is *not* an energy shifted replica of A but has significantly different features. D, Running integral of C. Significant current flow occurs at three different energies as indicated by the three distinct steps.

qualitatively and that the energy and *number* of hole transport channels is modified significantly by the transverse momentum change. For electron transport one would only observe almost identical step functions that are shifted in energy according to the transverse dispersion. The running integral shown in Fig. 7D is clearly not a shifted version of the integral shown in Fig. 7B. The Tsu–Esaki approximation to the transverse momentum integration (eqn (6)) is therefore expected to break down completely.

5.2. Hole transport current–voltage characteristics

With the discussions in the previous sections it is fairly clear that the current density $J(k)$ can be expected to have significant features in it. Figure 8 represents two of the central results of this paper: (1) the current density $J(k)$ can be sharply spiked outside the zone center Γ at $k \neq 0$ indicating that more holes traverse the structure at an angle than straight through, similar to an indirect bandgap material, and (2) to capture this physics one must perform an explicit integration over the transverse momentum.

Figure 8A shows two I–V characteristics computed at 4.2 K with (solid curve, eqn (2)) and without (dashed curve, eqn (6)) explicit integration over the transverse momentum on a logarithmic scale. The full integration with the transverse momentum shows a significantly enhanced current flow and current features that do not even show up in the analytic transverse integration. The origin of these additional channels is depicted in the color contour plot of the current density $J(k)$ of eqn (4) as a function of k and applied voltage

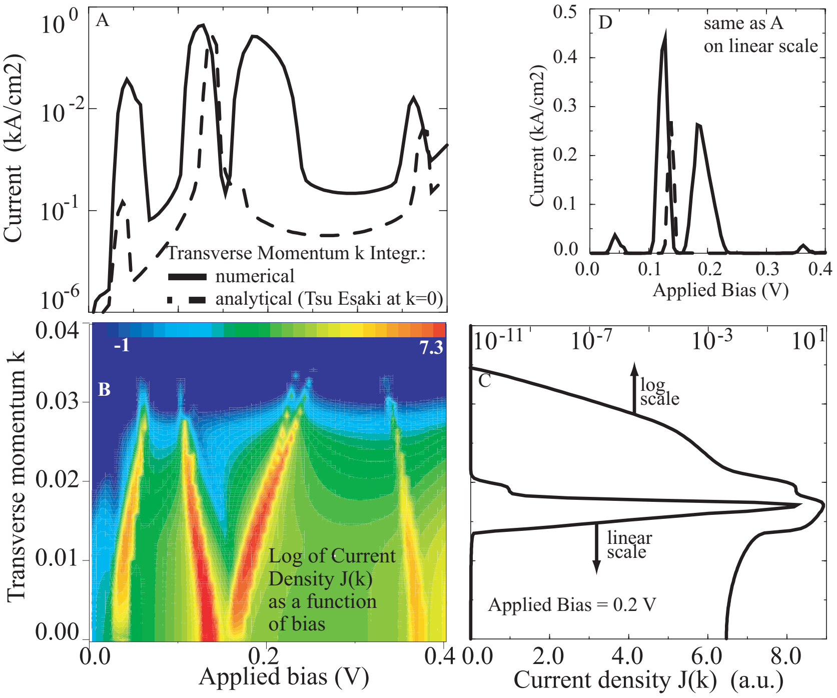

Fig. 8. A, I–V characteristic computed in the sp3s* model using numerical (solid curve) and analytical (dashed curve) transverse momentum integration. B, Logarithm of the current density integrand $J(k)$ as a function of applied bias and transverse momentum. The dashed line of A corresponds to a cut (except for scaling by the 2D density of states ρ_{2D}) through B along the $k = 0$ line. C, Vertical cut of $J(k)$ through B at a bias of 0.2 V on a horizontal logarithmic and linear scale. D, Same as A on a linear scale.

in Fig. 8B. Sharply defined streaks of current flow are visible in the momentum space. The current streaks resemble the transverse subband dispersion if the voltage axis is converted into an energy axis (with a factor of 0.5, due to the linear potential drop).

The key information to take from Fig. 8 is to realize that the current density $J(k)$ has maxima that are *not* at $k = 0$. This is shown explicitly by a cut through the contour plot at a constant voltage of 0.2 V in Fig. 8C. The current density is sharply peaked at a transverse momentum of about $k = 0.016$ as visible on a linear and logarithmic scale. These sharp peaks are completely ignored in the analytical Tsu–Esaki integration. In fact the dashed curve in Fig. 8A can be considered a cut through the contour of Fig. 8B at a constant transverse momentum $k = 0$. Figure 8D emphasizes the importance of the full band integration one more time by showing the I–V characteristic from Fig. 8A on a linear scale.

6. An analytic expression for the current density $J(k)$

6.1. Derivation

While the numerical simulation results appear acceptable, they do not provide good physical insight into the processes that generate the off-zone-center current flow. To better understand the behavior of the current density $J(k)$ as a function of the transverse momentum k an analytic expression is derived. The formula is derived by starting from eqn (2) assuming a Lorentzian shaped transmission coefficient of the form

$$T(E,k) = \frac{1}{1 + \left(\frac{E - E_r(k)}{\Gamma(k)}\right)^2}, \tag{7}$$

where $E_r(k)$ and $\Gamma(k)$, the momentum-dependent resonance energy, and resonance linewidth, are assumed to be independent of the transverse momentum direction, ϕ, for simplicity. Also for simplicity we assume zero temperature and that the bias is high enough to neglect back injection from the collector ($f_R = 0$). In the case of electron flow above the momentum-dependent conduction band edge $E_c(k)$ one can the write:

$$J(k) \propto u(E_F - E_c(k)) \int_{E_c(k)}^{E_F} \frac{dE}{1 + \left(\frac{E - E_r(k)}{\Gamma(k)}\right)^2} \tag{8}$$

$$= u(E_F - E_c(k))\, \Gamma(k) \left(a\tan \frac{E_r(k) - E_c(k)}{\Gamma(k)} - a\tan \frac{E_r(k) - E_F}{\Gamma(k)} \right) \tag{9}$$

where u is the Heaviside function. Reversing the energy scales results in a similar expression for $J(k)$ for holes.

6.2. $J(k)$ in identical, parabolic bands

To gain more analytical insight we now assume a perfect parabolic dispersion ($E_r(k) = E_0 + \frac{\hbar^2 k^2}{2m^*}$ and $E_c = \frac{\hbar^2 k^2}{2m^*}$) and a momentum-independent resonance linewidth ($\Gamma(k) = \Gamma_0$). Equation 9 can then be simplified to:

$$J(k) \propto u(E_F - E_c(k))\, \Gamma_0 \left(a\tan \frac{E_0}{\Gamma_0} - a\tan \frac{E_0 + \frac{\hbar^2 k^2}{2m^*} - E_F}{\Gamma_0} \right). \tag{10}$$

Under the assumptions leading to eqn (10) one can now show that $J(k)$ is monotonically decreasing as a function of transverse momentum for $E_c < E_F$:

$$\frac{dJ(k)}{dk} \propto -\frac{k}{1 + \left(\frac{E - E_r(k)}{\Gamma(k)}\right)^2} < 0. \tag{11}$$

We therefore confirm the intuitive result that the current density $J(k)$ is peaked at zero transverse momentum k and decreases monotonically with k. Note that this conclusion is only true for the restrictions of perfect and identical parabolic dispersion in the resonance energy and the conduction band edge (the lower bound for carrier injection).

6.3. Zone center current flow for electrons

To examine the derived analytical eqns (9) and (10) for $J(k)$ and to validate our numerical NEMO machinery for $J(k)$ we now compare the two for the electron RTD discussed previously in Section 4.4. Figures 9A and B show the I–V characteristic[†] on a linear and logarithmic scale, respectively, computed with (solid curve) and without (dashed curve) explicit transverse momentum integration at a temperature of 4.2 K. The analytical Tsu–Esaki integration and the numerical integration give virtually the same result with an increasing deviation for increasing voltages. This can be expected since the nonparabolicity overall is weak but increases at higher energies as indicated in Fig. 6B. Again we refer the reader to the discussion of the validity

---

[†] For simplicity and ease of comparison we use a linear potential drop in this computation as well as the hole simulation. This simulation is *not* meant to quantitatively predict the current through a GaAs/AlGaAs RTD.

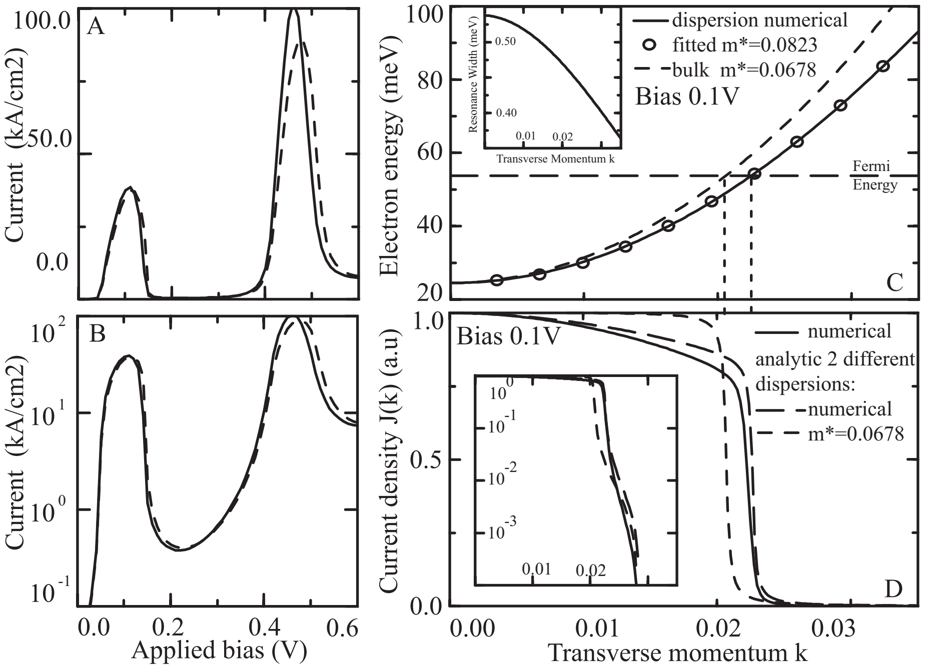

Fig. 9. A, I–V characteristic for a electron GaAs/AlGaAs RTD as described in the text. Solid and dashed curves show numerical and analytical integration of the transverse momentum, respectively. B, Same as A on a logarithmic scale. C, Transverse subband dispersion at the peak I–V of 0.1 V obtained numerically (solid curve), fitted with effective mass 0.0823 (open circles), and bulk effective mass 0.0678. Inset shows weak dependence of the resonance linewidth on the transverse momentum. D, Numerical $J(k)$ compared to analytical eqn (9) (long dash, with numerical E_r and Γ from (c)) and eqn (10) (short dash, with analytical E_r based on $m^* = 0.0678$). Current cut-off (indicated by vertical lines connecting C and D corresponds to the crossing of the resonance energies above the Fermi level in the emitter (horizontal dashed line in C). Inset shows the same curves on a logarithmic scale.

of the Tsu–Esaki formula in Section 3. The agreement between the Tsu–Esaki and full momentum integration in this case is purely due to the unphysical flat band in the emitter which produces 3D to 2D electron tunneling.

Figure 9C shows the transverse subband dispersion of the RTD ground state at the first resonance voltage of 0.1 V. The numerical dispersion (solid curve) can be fitted to an effective mass of 0.0823 (empty circles) which is slightly heavier than the bulk effective mass for this bandstructure model of 0.0678 (dashed curve). This slightly heavier mass is another indication of the band nonparabolicity mentioned above. The inset in Fig. 9C shows the relatively weak dependence (20%) of the ground state linewidth as a function of transverse momentum. The dashed horizontal line indicates the Fermi level in the emitter. This horizontal line can be thought of as the fill level of the subbands. The subbands are full of electrons below this level and empty above. Figure 9D compares the numerical curve of $J(k)$ obtained with NEMO at a bias of 0.1 V to two curves computed with eqn (9) (long dashed curve, Γ and E_r from Fig. 9C) and eqn (10) (short dashed curve, $m^* = 0.0678$, $E_0 \approx 22$ meV, and $\Gamma_0 \approx 0.57$ meV). The inset shows the same curves on a logarithmic scale. The three curves are indeed monotonically decreasing (see Section 6.2) with the peak at $k = 0$. All three show a particular sharp cut-off that can be associated with the rise of the resonance energy above the Fermi level as indicated by the vertical dashed lines connecting Figs 9C and D. It can be shown numerically [38] that for all bias points $J(k)$ is monotonically decreasing.

The qualitative and quantitative agreement of the zero temperature analytic expressions of eqns (9) and (10) with the purely numerical result at 4.2 K confirms the validity of the analytic equations and the numerical

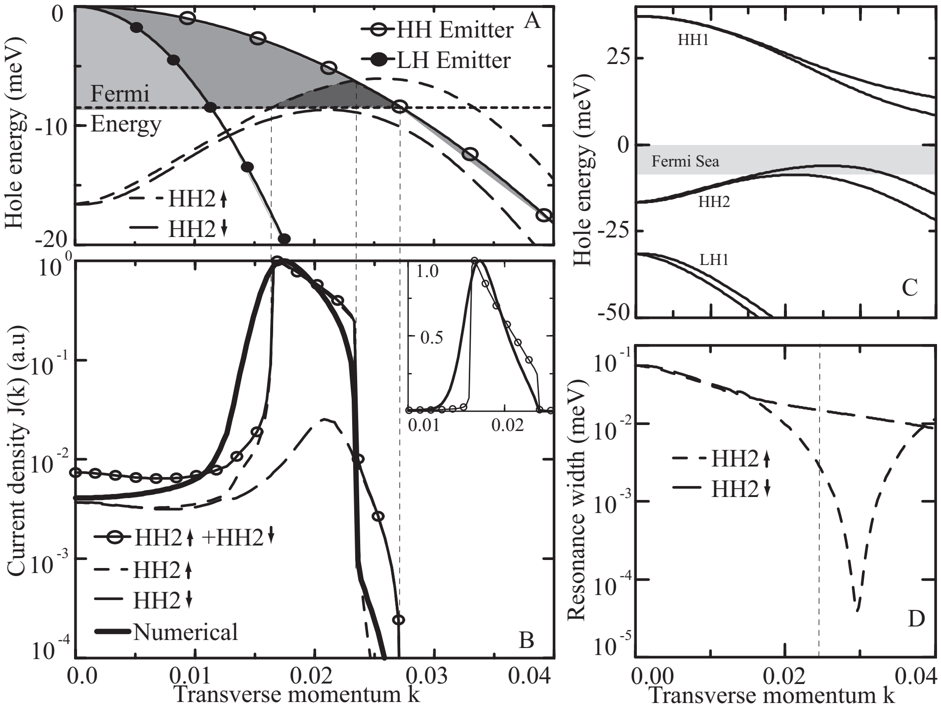

Fig. 10. A, Transverse dispersion of the HH2↑, ↓ states (dashed curves) at a bias of 0.113 V. Solid curves are the 3D HH and LH dispersions in the emitter filled with holes to the Fermi level (light gray area). Horizontal line is the emitter Fermi level. B, Numerical $J(k)$ (thick curve) compared to various analytic current components based on eqn (9): HH2↑ (short dash), HH2↓ (long dash) and the sum of the two (solid curve with circles). Inset: same as B on a linear scale. Sharp $J(k)$ turn-on at $k \approx 0.016$ corresponds to HH2 up-spin touching the Fermi sea. The first sharp cut-off corresponds to the HH2↑ state crossing the emitter subband. The current is carried completely by HH2↓. This current contribution turns off as the bulk emitter dispersion crosses the Fermi sea. C, Overview of the transverse hole dispersion under a bias of 0.113 V. The gray area indicates the occupied hole states in the emitter. D, Dependence of the resonance linewidths of HH2 states as a function of transverse momentum.

machinery in NEMO. Deviations between the analytical and numerical results are due to the zero temperature assumption of the analytical formulas. The following sections will utilize eqn (9) to analyze spectral features in $J(k)$ for hole transport.

6.4. Off-zone-center current flow due to nonmonotonic dispersion

The discussion of $J(k)$ for electron transport revealed the importance of the crossing of the dispersion curve with the Fermi level in the emitter for the cut-off of the current. With the nonmonotonic hole dispersions shown in Fig. 5 one can imagine that a resonance that is outside the Fermi sea at zero transverse momentum dips into it at $k > 0$ and then leaves the Fermi sea again as the transverse momentum is increased. This basic mechanism is the theme of Fig. 10 where the numerical $J(k)$ is compared to the analytical expression in eqn (10).

Figure 10C provides an overview of the energy scales of the subbands that might be involved in hole transport at a bias of 0.113 V (compare to Fig. 8). The emitter valence band edge is set to be the zero-energy origin. The emitter hole states are occupied in a narrow energy range below the valence band edge as indicated by the shaded area. The HH1 subband is pulled above the valence band edge and cannot conduct holes. The LH1 subband is too far below the Fermi sea to conduct. Only the HH2 subband is within reach of the shaded Fermi sea.

Figure 10A is an expanded view of Fig. 10C in the energy range around the Fermi sea. It shows the HH2 $\uparrow$ and HH2 $\downarrow$ dispersion as dashed curves. The solid curves with the circles indicate the HH and LH bulk dispersions of the emitter. The horizontal line indicates the hole Fermi level in the emitter.

Figure 10B compares the numerically obtained $J(k)$ (thick solid curve) to three components HH2 $\uparrow$, HH2 $\downarrow$, and the simple sum [26, 39] HH2 $\uparrow$ + HH2 $\downarrow$ computed with eqn (9) using the dispersion information about E_{F}, $E_{\mathrm{HH\ emitter}}$, and Γ in Fig. 10A and D.[†] The qualitatively excellent agreement between the numerical $J(k)$ and the HH2 $\uparrow$ + HH2 $\downarrow$ analytical result is quite striking.[‡]

At zero transverse momentum both states HH2 $\uparrow$ and HH2 $\downarrow$ are below the Fermi sea in the emitter. Only the long Lorentzian tails of the resonances conduct a current. The sharp turn-on at $k \approx 0.016$ can be associated with the HH2 $\uparrow$ touching into the Fermi sea due to the nonmonotonic dispersion. The current is dominantly carried by this channel. At a transverse momentum of $k \approx 0.0235$ the HH2 $\uparrow$ dispersion crosses the bulk (3D) HH in the emitter. Beyond that crossing point no energy and momentum conserving hole 3D to 2D transitions can be found and the HH2 $\uparrow$ channel turns off. Only the HH2 $\downarrow$ is left to conduct through its Lorentzian tail. This conduction channel is finally shut off as the bulk (3D) HH emitter dispersion is below the Fermi energy and cannot supply any more carriers at a transverse momentum of about $k \approx 0.027$.

Figure 10D shows the momentum dependence of the resonance linewidths Γ of HH2 that is needed for the evaluation of eqn (9). The HH1 $\uparrow$ shows an interesting large (three orders of magnitude) dependence of the resonance linewidth. A more detailed discussion of the resonance linewidth dependence is deferred to Appendix B.

Figure 10A shows the LH emitter dispersion for reference. If eqn (9) were to be used with the LH emitter dispersion instead of the HH dispersion for E_c one *could not* achieve the agreement between the analytic and the numerical $J(k)$ as shown in Fig. 10B. $J(k)$ would turn off at $k \approx 0.012$ at the crossing of the LH emitter subband with the Fermi level. The current flow at a bias of 0.113 is completely due to carriers that are injected from the HH states in the emitter.

Looking at Fig. 10 as a whole we can clearly see how the nonmonotonic behavior of the hole dispersion can create current features that are sharply spiked in the transverse momentum dependence. The following two sections will describe two other mechanisms that can generate similar spikes in $J(k)$.

6.5. Off-zone-center current flow due to different emitter and quantum well effective masses

The previous section discussed how a sharply spiked current density $J(k)$ at $k > 0$ can be generated by the nonmonotonic hole dispersion. The current turns on as the quantum well dispersion dips into the Fermi sea at $k > 0$. A current turn-off was observed when the well dispersion crossed the emitter dispersion. Quantum well and emitter dispersion crossings can occur even for simpler, almost parabolic, dispersions. In particular this can occur if the effective mass in the quantum well is significantly smaller than in the emitter. In Fig. 11 it is shown, how monotonic differently sloped dispersions can result in similarly spiked $J(k)$ current turn-ons and turn-offs. Similar to Fig. 10 the shape of the current density $J(k)$ is dominated by the crossings of the quantum well dispersions and the emitter dispersion with each other and the Fermi level in the emitter.

At a bias of 0.048 V the main current contribution is due to tunneling through the HH1 states as indicated in Fig. 11. The current through HH2 states must be included to explain the background current density of

---

[†] Instead of re-deriving a formula for the hole case we just change the sign on all the energy scales for the hole dispersions.

[‡] The agreement is particularly surprising considering that we simply add two Lorentzian shaped transmission channels, without performing a more exact expansion on the corresponding transmission coefficient [26, 39]. The deviation between the full numerical result and the semi-analytical result is associated with the simple Lorentzian lineshape and the zero temperature assumption.

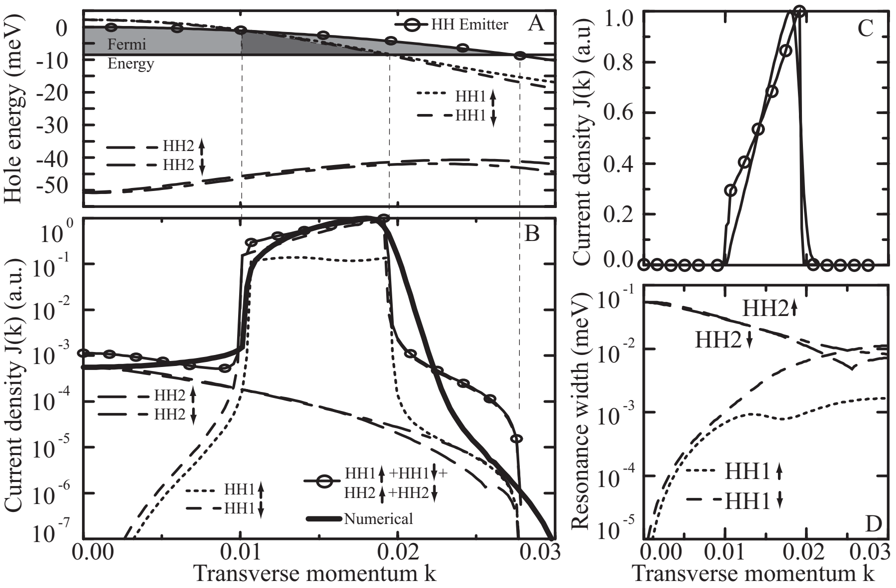

Fig. 11. A, Hole dispersion at a bias of 0.048 V (dashed curves). Emitter HH dispersion is indicated by the solid curve with circles filled with holes (light gray shades) up to the Fermi level. Crossings of the HH and emitter dispersion with each other and the Fermi level will result in features of $J(k)$ in B as indicated by vertical lines. B, Numerical $J(k)$ (thick solid curve) compared to four analytical contributions computed from A and D using eqn (9). Current peak is carried by HH1 states as they pass through the emitter injection dispersion and the Fermi sea. The background current is carried by the HH2 states which have a significant broader linewidth than the HH1 states. C, same as B on a linear scale. D, Resonance linewidths as a function of transverse momentum of the four lowest HH states.

$J(k)$ that is not due to the HH1 states. The dramatically different resonance widths of the HH1 and HH2 states are shown in Fig. 11D. A more detailed discussion of the dependence of the resonance widths on transverse momentum and bias is deferred to Appendix B. The four analytic current contributions are simply added up assuming independent Lorentzian lineshapes [26, 39]. The agreement between the numerically and analytically obtained $J(k)$ in their shape over several orders of magnitude is astonishing.

Similar to the case at 0.113 V in the previous section, we again find at the bias of 0.048 V that the current flowing through the structure is dominated by the HH emitter injection.

The phenomenon of crossing quantum well and emitter dispersions is not limited to hole transport, but it is indeed quite common for high-performance InP-based resonant tunneling diodes [40] where the well might contain InAs, while the emitter is typically InGaAs with a larger effective mass [41, 42]. We have seen this effect of nonzone center current flow in direct bandgap electron devices in such InGaAs/AlAs/InAs high-performance RTD systems.

6.6. Off-zone-center current flow due to resonance linewidth modulations

The previous two sections explained how crossings between emitter dispersion, quantum well dispersion, and emitter Fermi level can lead to current flow that is dominant (sharply peaked) off the zone center in a narrow momentum space. This section will demonstrate how the strong dependence of the resonance linewidth can induce similar off-zone-center current flow.

The insert in Fig. 12C shows the dispersion of the lowest eight states at a bias of 0.168 V. The shaded area indicates the width of the Fermi sea in the emitter from which holes can be injected. Only the LH1 states are in the energy range that can provide significant conductance through the structure. Figure 12A shows the LH1, HH emitter, and LH emitter dispersions as well as the emitter Fermi level. Given this dispersion one can

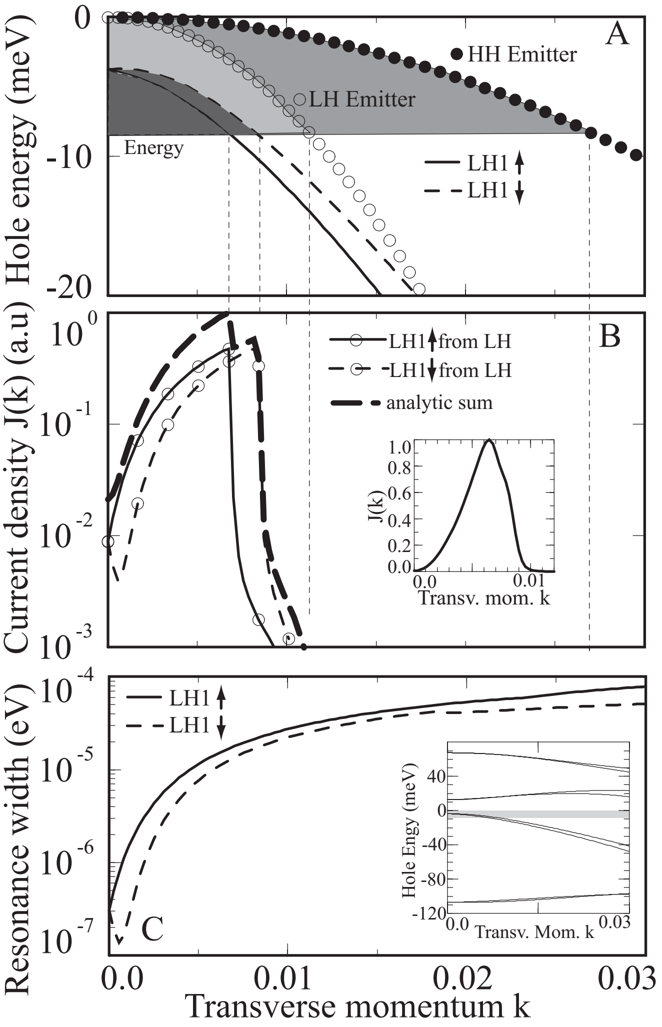

Fig. 12. A, LH1 dispersion at a bias of 0.168 V. Emitter HH and LH dispersion is indicated by the filled and open circles, respectively. The filling of the emitter dispersions up to the Fermi level is indicated by the light gray areas. Crossings of the dispersions at the Fermi level will result in *turn-off* features of $J(k)$ in B as indicated by vertical lines. Holes which can tunnel through the device are indicated by the dark gray area. B, Numerical $J(k)$ (thick solid curve) compared to four analytical contributions computed from A and C using eqn (9). The HH emitter injection is weighed by a scaling factor of 0.2. The current turn-on is associated with the strong modulation of the resonance width as a function of momentum shown in C. The inset in B is the same as B on a linear scale. The inset in C is an overview of the quantum well dispersion at this bias. The gray shade indicates the Fermi sea.

expect current flow through the LH1 state by injection from either the LH or HH states in the emitter. Current flow is expected to cease as a function of transverse momentum as the quantum well and emitter dispersions are leaving the Fermi sea, similar to the electronic case presented in Fig. 9. Therefore a monotonically decreasing current density similar to Fig. 9D could be expected. However, the resonance widths, Γ, of the LH1 states show (see Fig. 12C) an increase by over two orders of magnitude in the transverse momentum range of interest. This increase in Γ leads to a dramatic increase in the current density $J(k)$ as indicated in Fig. 12B.

Unlike the previous two sections where only the carrier injection from the HH emitter dispersion needed to be considered, carrier injection from both, the HH and LH dispersion in the emitter is considered in this case (full and open circles, respectively). The emitter HH contribution is weighed by an arbitrary factor of 0.2 compared to the emitter LH contribution to best match the lower lying shoulder at $k > 0.02$. At a bias of 0.168 V most of the current is due to injection from the LH emitter subband. Injection from the HH emitter subband only provides a background that is visible on the logarithmic scale of Fig. 12B.

Note that the turn-on in $J(k)$ appears smoother on a linear scale (inset of Fig. 12B) compared to the previous cases (see the inset in Fig. 10B and Fig. 11C). This is due to fact that the turn-on is generated by the smooth increase in the resonance linewidth Γ and not by a crossing of the various dispersions with the Fermi level. Also in this case the agreement between the numerical and the semi-analytical $J(k)$ is quite remarkable.

6.7. Current flow dominated by HH injection

The previous three sections showed for three different bias points that the current flow through HH/LH states in the quantum well is dominated by injection from HH/LH states in the emitter, respectively. The purpose of this section is to show that this same-state-injection dominance is in general not true, but that the current is mostly dominated by HH injection from the emitter over a large voltage range.

Figure 13A compares I–V characteristics calculated completely numerically with NEMO and analytically from eqn (9). To obtain an I–V across a voltage range using eqn (9) one must have a complete transverse dispersion including the resonance energy as well as the resonance linewidth as a function of bias. The dispersion may change beyond the simple shift in energy with the applied bias due to the changing coupling to the leads as the emitter/collector barrier becomes more/less opaque with increasing bias. This change in coupling will mostly affect the resonance widths. (For a more detailed discussion of the bias dependence of the dispersion see Appendix A and B.) Instead of using NEMO to compute the dispersion at every bias point we have used only two dispersions at a bias of 0 V and 0.2 V and interpolated from these dispersions for all the bias points in the voltage range 0–0.3 V and applied the simple shift in energy of half the applied voltage in electron volts due to our simple linear drop potential.

In the application of eqn (9) we have included the lowest eight resonances and have treated them independently of each other assuming a Lorentzian lineshape as we have done in the previous three sections. All the resonances are assumed to couple equally[†] to the LH and the HH emitter states. The complete analytic and numerical I–V characteristics are normalized to a peak value of one. The good agreement between full numerical solution and the analytic solution based on eqn (9) is astonishing.

The thin dashed curve shown in Fig. 13A shows the analytic current contribution due to emitter LH band injection only. Considering the LH injection alone underpredicts the current by several orders of magnitude, we therefore conclude that most of the current is carried due to HH emitter injection. This is somewhat of a surprise since the barriers are much more opaque for HHs than LHs. This dominance of the HH injection underlines the importance of the band mixing due to the heterostructure interface.

Figure 13B and C show the dependence of the current density $J(k)$ versus applied voltage and transverse momentum for HH and LH injection computed from eqn (9). The HH/LH injection $J(k)$ cut-off at a transverse momentum of 0.012/0.027, respectively, corresponds to the crossing of the LH/HH emitter with the Fermi level (see, for example, Fig. 12).

The solid curves in these plots show the first k-moment ($k_J = \int_0^1 kJdk / \int_0^1 Jdk$) of the current density in the transverse direction. Off-zone-center current flow dominates wherever the first moment exactly follows the center of the distribution (red streaks). The dominant current flow is at the zone center when the first

---

[†] Unlike the single example shown in Section 6.6.

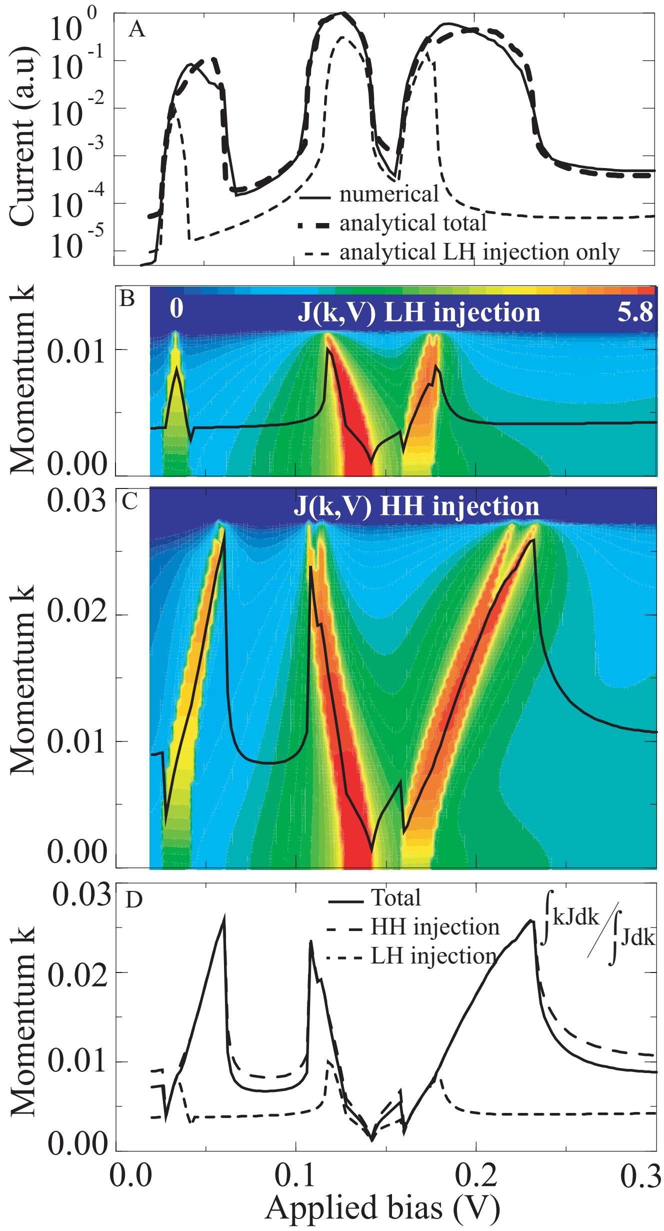

Fig. 13. A, I–V characteristic normalized at a peak current of one. Solid curve identical to solid curve in Fig. 8A computed with NEMO. Thick dashed curve computed from analytic eqn (9). Thin dashed curve only LH emitter injection. B, C, Log of $J(k)$ as a function of voltage from analytic eqn (9) for LH, HH emitter injection. Black curves show the first moment of $J(k)$ defined as $k_J = \int_0^1 kJdk / \int_0^1 Jdk$. D, k_J computed for the individual injections from LH and HH and the total injection.

moment is independent of the voltage. From Fig. 13C one can therefore conclude that the current flow is off-zone-center for most of the bias range.

Figure 13D compares the two individual first moments of $J(k)$ from Fig 13B and C to each other and to the first moment of the total current density. Again the dominance of the HH injection over the LH injection is dramatically displayed. Also, this figure shows again the extent of the voltage region in which the current flow is dominated by off-zone-center processes.

This section presents an I–V calculation that is purely based on the analytic eqn (9) and two numerical dispersions at biases of 0 and 0.2 V. This procedure speeds up the time needed to compute a single I–V simulation by at least three orders of magnitude. This speed-up enables us to compute multiple I–V characteristics for various parameters that do not change the central resonance dispersion.

7. Fermi level dependence

Sections 6.4–6.7 show that the crossing of the various central resonance and emitter subband dispersions with the Fermi level in the emitter produce sharp turn-ons and turn-offs in the current density $J(k)$ and ultimately in the fully integrated current. All the previous discussions assume a fixed Fermi level of 8.4 meV. This section examines the dependence of the overall current on the Fermi level in the emitter. The current is computed using the same semi-analytical approach as presented in the previous section. Figure 14A shows two I–V characteristics computed for Fermi energies of 5 and 20 meV. The increase of the Fermi level clearly raises the overall current by more than one order of magnitude. It also broadens out the individual current peaks significantly. That effect can be associated with the much larger k-space in which transport through nontrivial subbands can take place. This trend is strikingly similar to the two I–V characteristics shown in Fig. 8A which discussed the proper integration over the k-space. Again we can show the Tsu–Esaki approximation to be limited to a small Fermi level. The overall increase in the current with the Fermi level increase is understandable in the context of an increased occupied k-space in the emitter.

Figure 14B shows the spreading out and increased amplitude of the current peaks in a contour plot as a function of Fermi energy. The current turn-ons move to smaller voltages with increasing Fermi levels as expected, since the resonances touch the Fermi sea at smaller voltages. However, the different states show two different turn-off dependencies with the Fermi level. The turn-off of the second and fourth current peak (HH2 and HH3) are independent on the Fermi level while the turn-offs of the first/third current peak HH1/LH1 show a weak/strong dependence, respectively. These HH1/LH1 turn-offs move to higher voltages. This behavior can be understood in terms of turn-ons and turn-offs of $J(k)$.

Figure 11A shows that the $J(k)$ turn-off of the HH1 state (first current peak in Fig. 14B) is determined by the crossing of the resonance subband with the Fermi energy. As the Fermi energy is increased the turn-off moves to a larger transverse momentum which in turn increases the area under the curve $J(k)$ (Fig. 11B). The $J(k)$ turn-on is determined by the crossing of the central resonance with the HH emitter dispersion where the central effective mass is smaller than the emitter effective mass. Increasing the Fermi level increases the voltage range where such a turn-on can happen before the dispersions have crossed the Fermi level. The effect is larger for the LH1 state than the HH1 state since the difference to the HH emitter mass is more significant.

The turn-offs of peaks 2 and 4 in Fig. 14 are independent of the Fermi level since these peaks correspond to HH2 and HH4 which are characterized by an almost flat transverse dispersion (see Fig. 5B). Their condition for current turn-off in $J(k)$ is not influenced by the Fermi level.

8. Current–voltage temperature dependence

All of the I–V characteristics discussed in the previous sections were computed at a temperature of 4.2 K. As the hole temperature is increased for a given Fermi level, more holes are thermally excited above the Fermi

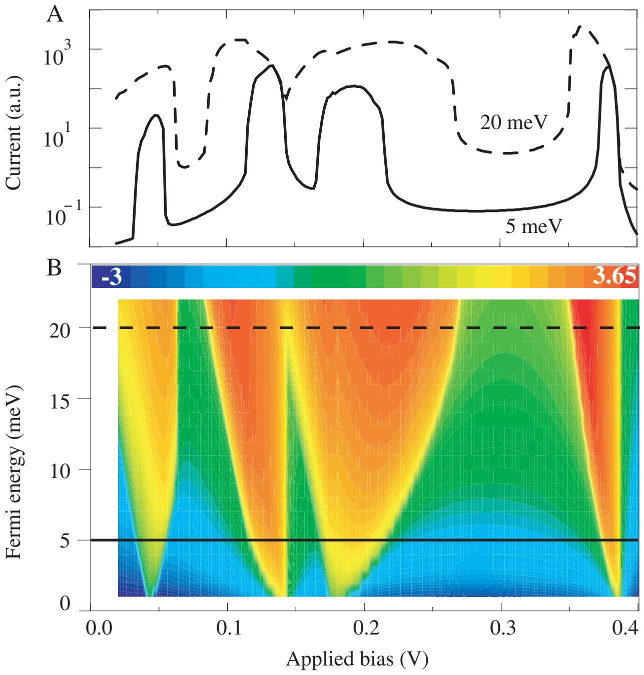

Fig. 14. A, I–V characteristic for two different emitter Fermi levels (5 and 20 meV). B, Logarithm of I–V characteristics as a function of Fermi energy.

level in total energy E as well as transverse momentum k. The $k \approx 0.027$ cut-off of $J(k)$ at a temperature of 4.2 K (see Fig. 8), is pushed to about $k \approx 0.08$ at a temperature of 300 K. This increased range of carrier injection in the transverse momentum space increases the number of channels that can propagate holes through the structure significantly. This increased number of transmission channels is expected to wipe out most of the I–V features that are visible at 4.2 K. Figure 15 shows a comparison of three different I–V characteristics computed at 4.2, 77, and 300 K. Indeed it is found that most of the sharp current features vanish. However, this does not take away from the conclusion that most of the current is transported away from the zone center. Indeed we verified (not shown here) in a plot similar to Fig. 8B that the current $J(k)$ peaks outside the zone center.

9. Transverse momentum angle dependence

All of the previous discussions have considered the dependence of the carrier transport on the magnitude of the transverse momentum $\boldsymbol{k}$, however the dependence on the angle ϕ has been omitted. In all the previous discussions the transverse momentum was considered only in the [100] direction corresponding to $\phi = 0$. Due to the rotational symmetry of the GaAs (zincblende) lattice one can expect a rotational symmetry every 90°[†] with a mirror plane symmetry along [110]. Figure 16 shows the transverse hole dispersion for these two extremal momentum directions $\phi = 0$ and $\phi = 45$. The subband dispersion appears to be only weakly dependent on the angle ϕ.

Figure 17 examines the I–V characteristic dependence on the transverse momentum angle ϕ. Figure 17A

[†] Zincblende is invariant under a rotation of 90° about x, y, or z, followed by a reflection in the plane of rotation (plane normal to the axis of rotation).

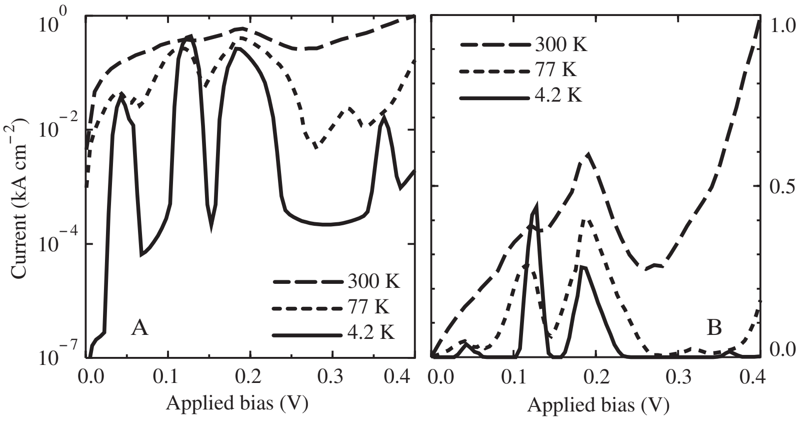

Fig. 15. A, I–V characteristic computed for three different temperatures, 4.2, 77, and 300 K on a logarithmic scale. B, Same as A on a linear scale.

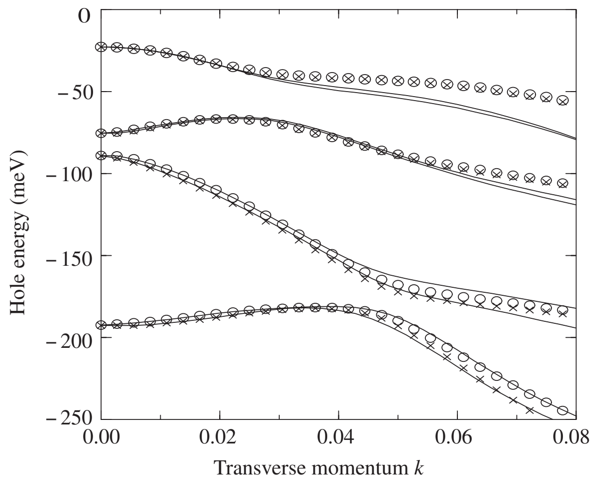

Fig. 16. Hole dispersion for $\phi = 0$ (solid curves) and $\phi = 45$ (symbols).

shows three different I–V characteristics: two computed at a fixed $\phi = 0$ and $\phi = 45$ using eqn (2) and one based on an explicit integration over the ϕ coordinate using eqn (1). Only a small dependence on the angle ϕ can be found in the current peak that can be associated with the LH1 resonance. Figure 17B verifies this weak dependence on the angle ϕ in a contour plot over the angle range of $[0 \ldots 45]$ with nine steps of size 5.625. This is the raw data that lead to the integration over the angle ϕ in Fig. 17A.

From Figs 16 and 17 one can conclude that the assumption of angular symmetry that leads from eqn (1) to eqn (2) is well satisfied in the model system considered here. Only a relatively weak dependence on the angle ϕ is found. Only the third current peak (LH1) shows a weak dependence on the angle of incidence. A stronger dependence could be expected in cases where more holes are injected at larger transverse momentum magnitude, since that is where the dispersion differs more significantly. We checked this hypothesis by comparing I–V characteristics computed at various angles at a temperature of 300K. However, only a small dependence on the transverse momentum angle was found as well (not shown in a figure here).

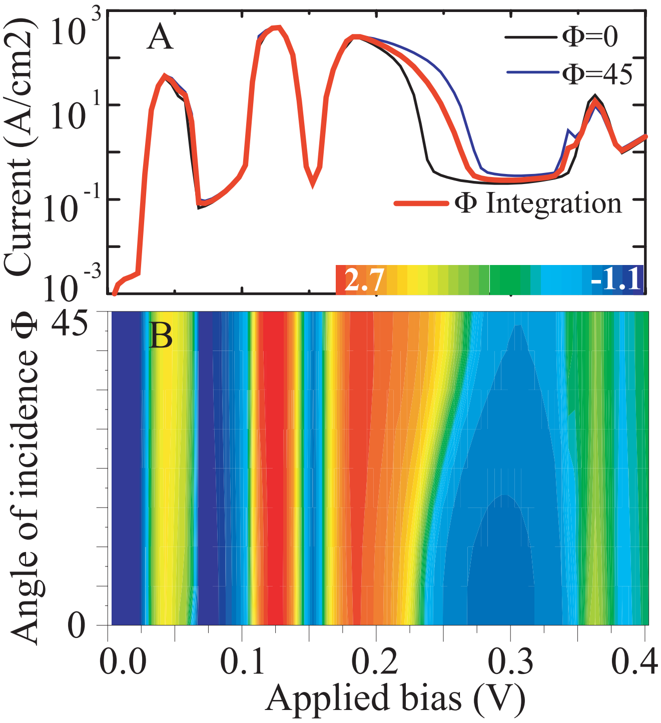

Fig. 17. Angular dependence of the resonant tunneling current. A, I–V characteristic computed with eqn (2) with $\phi = 0$ (black curve), with $\phi = 45$ (blue curve), and full ϕ integration with eqn (1) (red curve). B, Current density $J(\phi)$ as a function of applied voltage.

10. Comparison against experiment

Hole resonant tunneling diodes have been investigated experimentally in some detail [44]. Negative differential resistance and effects due to charge accumulation in the central RTD and emitter region have been observed in a variety of different structures. Our previous research on electron transport RTDs has shown [4–7] that the proper modeling of the free charges inside and outside the central RTD are essential in the quantitative prediction of the I–V characteristics. To simplify the comparison against experimental data we pick an experimental data set that is weakly dependent on the charge accumulation *inside* the central RTD. Hayden *et al*. [44] studied the effect of charge accumulation and intrinsic bi-stability in an asymmetric RTD. Their structure is described as ‘a 4.2-nm GaAs quantum well formed between two AlAs tunnel barriers of thickness 4.5 and 5.7 nm. Undoped spacer layers of thickness 5.1 nm separate the two tunnel barriers from Be-doped contact layers in which the doping is graded from $5 \times 10^{17}\text{cm}^{-3}$ to $2 \times 10^{18}\text{cm}^{-3}$ over a distance of 200 nm’. The mesa size is assumed[†]to be 100 μm. Figure 18 shows the forward bias data taken from Fig. 2 of Ref. [44] in a solid line on two different voltage scales. In that bias direction no charge accumulation is evident in the central RTD since the escape rates through the collector barrier (4.5 nm) is larger than the entry rate through the emitter barrier (5.7 nm). NEMO allows the user to choose a variety of different electrostatic potential models. The Thomas–Fermi model assumes a semi-classical free charge distribution in the leads and a zero free charge in the nonequilibrium region. This model leads to simulation results [4, 7] that provide reasonable insight into the device performance as long as the charge accumulation in the RTD is negligible. Effects due

---

[†] R. K. Hayden, private communication. The mesa sizes used in the experiment have diameter of 100 μm.

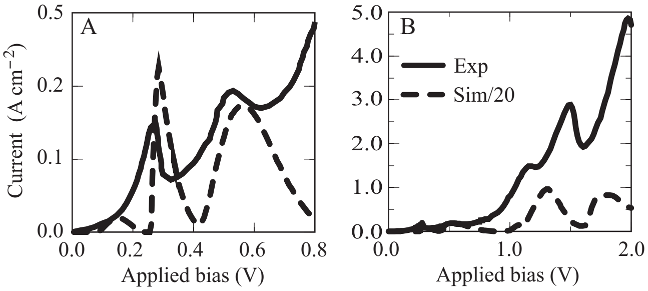

Fig. 18. A, I–V characteristic (solid curve) for an asymmetric hole RTD from Ref. [44] compared to our simulation result scaled down by a factor of 20.0 (dashed curve). B, Same as A in a larger voltage range.

to the quantization in the emitter notch [4, 44] are neglected in the free charge calculation. The Hartree charge self-consistent potential model was not used in the simulations shown here to reduce the required CPU time.

We entered the structure as described by Hayden *et al.* [44] into NEMO, chose an optical relaxation rate of 24 meV in the contact regions [4], and used the same second-nearest neighbor sp3s* model as in the rest of this paper. The resulting I–V characteristic is compared to the experimental data in Fig. 18. The simulation results have to be scaled down by a factor of 20.0 to be compared to the experimental data on a linear scale. While such a deviation might sound large we point out here that such a deviation is not completely unexpected. We have verified with NEMO that variations of 2–3 monolayers in the barrier thickness and variations in the doping profile detail can result in such current density variations of factors of 20. We feel that such deviations can only be eliminated in a controlled test matrix [6] of experimental structures where experimental trends can be analyzed in more detail. Such a controlled comparison between experiment and theory is not the point of this paper here.

One question raised by Hayden [44] was the lack of a HH1 resonance in the I–V spectrum. Our simulations suggest that the HH1 peak is in the scattering enhanced large tail of the HH2/LH1 peak.

The main point of the paper that the dominant current flow through the structure occurs at $k \neq 0$ has been verified for the experimental structure with a similar plot to Fig. 8B (not shown here). A Tsu–Esaki-type analytical integration cannot possibly provide the proper insight into the transport channels through this experimental structure. This point can also be made by plotting the data on a logarithmic scale [43] similar to Fig. 8A together with a Tsu–Esaki integration result.

The comparison in Fig. 18 shows clearly that the simulation is clearly deviating from the experimental results in the valley currents. We attribute this to the lack of incoherent scattering in the central RTD in our simulation. At this stage NEMO can only simulate interface roughness, polar optical phonon, acoustic phonon and alloy disorder scattering in a single-band model [8–10]. Such a single-band model is, however, incapable of incorporating the HH, LH and SO hole band interactions which are the first-order effects that establish the coherent channels through the central RTD.

For pure electron transport in RTDs it has been shown [8–10] that at low temperatures bandstructure effects are negligible and scattering processes due optical phonons and interface roughness are dominant. As an overall conclusion to the the comparison to experimental data we submit that at low temperatures the inclusion of full bandstructure (not just single bands) and scattering is essential to completely model the current flow through a hole RTD.

11. Summary

This work demonstrates four key findings: (1) the HH and LH interaction is shown to be strong enough to result in dominant current flow off the Γ zone center, (2) explicit inclusion of the transverse momentum in the current integration is needed, (3) most of the current flow is due to injection from HHs in the emitter, and (4) the dependence on the transverse momentum angle ϕ is weak. An analytic formula for the current density $J(k)$ as a function of transverse momentum k has been derived and utilized to explain the three mechanisms that generate off-zone-center current flow: (1) nonmonotonic (electron-like) hole dispersion, (2) different quantum well and emitter effective masses, and (3) momentum-dependent quantum well coupling strength. The analytic expression is also used to generate a complete I–V characteristic that compares well to the full numerical solution based on two single transverse subband dispersions at different voltages. The Fermi level and temperature dependence on the I–V is examined. From a comparison of a simulation to experimental data it is concluded that the inclusion of full bandstructure as well as incoherent scattering is needed to completely model I–V characteristics in RTDs.

Acknowledgements—The work described in this publication was carried out by the Jet Propulsion Laboratory, California Institute of Technology under a contract with the National Aeronautics and Space Administration. The supercomputer used in this investigation was provided by funding from the NASA Offices of Earth Science, Aeronautics, and Space Science. Part of the research reported here was performed using HP SPP-2000 operated by the Center for Advanced Computing Research at Caltech; access to this facility was provided by Caltech.

GK and RCB would like to acknowledge the careful review of the manuscript and valuable comments by Marc Cahay. GK acknowledges the careful review of the manuscript by Fabiano Oyafuso.

References

[1] See `http://hpc.jpl.nasa.gov/PEP/gekco/nemo` or search for NEMO on `http://www.raytheon.com`.
[2] R. Lake, G. Klimeck, R. C. Bowen, and D. Jovanovic, J. Appl. Phys. **81**, 7845 (1997).
[3] R. Lake *et al*., Phys. Status Solidi (b) **204**, 354 (1997).
[4] G. Klimeck *et al*., Appl. Phys. Lett. **67**, 2539 (1995).
[5] R. Lake, G. Klimeck, R. C. Bowen, C. Fernando, D. Jovanovic, D. Blanks, T. S. Moise, Y. C. Kao, M. Leng, and W. R. Frensley, *54th Annual Device Research Conference Digest* (IEEE, NJ, p. 174.
[6] G. Klimeck, T. Boykin, R. C. Bowen, R. Lake, D. Blanks, T. S. Moise, Y. C. Kao, and W. R. Frensley, *1997 55th Annual Device Research Conference Digest* (IEEE, NJ, p. 92.
[7] R. C. Bowen *et al*., J. Appl. Phys. **81**, 3207 (1997).
[8] R. Lake *et al*., Superlatt. Microstruct. **20**, 279 (1996).
[9] R. Lake, G. Klimeck, and D. K. Blanks, Semicond. Sci. Technol. **13**, A163 (1998).
[10] G. Klimeck, R. Lake, and D. K. Blanks, Phys. Rev. **B58**, 7279 (1998).
[11] E. E. Mendez, W. I. Wang, B. Ricco, and L. Esaki, Appl. Phys. Lett. **47**, 415 (1985).
[12] R. K. Hayden *et al*., Phys. Rev. Lett. **66**, 1749 (1991).
[13] J. A. Kash, M. Zachau, M. A. Tischler, and U. Ekenberg, Phys. Rev. Lett. **69**, 2260 (1992).
[14] W.-C. Tan, J. C. Inkson, and G. P. Srivastava, Phys. Rev. **B54**, 14623 (1996).
[15] J. M. Luttinger and W. Kohn, Phys. Rev. **97**, 869 (1955).
[16] M. Burt, Semicond. Sci. Technol. **3**, 739 (1988).
[17] B. Foreman, Phys. Rev. Lett. **81**, 425 (1998).
[18] S. Ekbote, M. Cahay, and K. Roenker, Phys. Rev. **B58**, 16315 (1998).
[19] S. Ekbote, M. Cahay, and K. Roenker, J. Appl. Phys. **87**, 1467 (2000).
[20] C. Y.-P. Chao and S. L. Chuang, Phys. Rev. **B43**, 7027 (1991).
[21] Y. X. Liu, R. R. Marquardt, D. Z.-Y. Ting, and T. C. McGill, Phys. Rev. **B55**, 7073 (1991).
[22] J. X. Zhu, Z. D. Wang, and C. D. Gong, Solid State Commun. **101**, 257 (1997).
[23] M. S. Kiledjian, J. N. Schulman, K. L. Wang, and K. V. Rousseau, Phys. Rev. **B46**, 16012 (1992).

[24] M. S. Kiledjian, J. N. Schulman, K. L. Wang, and K. V. Rousseau, Surf. Sci. **267**, 405 (1992).
[25] T. Boykin, L. J. Gamble, G. Klimeck, and R. C. Bowen, Phys. Rev. **B59**, 7301 (1999).
[26] R. C. Bowen, W. R. Frensley, G. Klimeck, and R. K. Lake, Phys. Rev. **B52**, 2754 (1995).
[27] J. P. A. van der Wagt, A. C. Seabaugh, and E. Beam III, IEEE Electron Device Lett. **19**, 7 (1998).
[28] T. P. E. Broekaert *et al.*, IEEE J. Solid-State Electron. **33**, 1342 (1998).
[29] G. Klimeck *et al.*, VLSI Des. **6**, 107 (1998).
[30] R. Tsu and L. Esaki, Appl. Phys. Lett. **22**, 562 (1973).
[31] T. B. Boykin, R. E. Carnahan, and R. J. Higgins, Phys. Rev. **B48**, 14232 (1993).
[32] T. B. Boykin, R. E. Carnahan, and K. P. Martin, Phys. Rev. **B51**, 2273 (1995).
[33] T. B. Boykin, J. Appl. Phys. **78**, 6818 (1995).
[34] U. Fano, Phys. Rev. **124**, 1866 (1961).
[35] O. Madelung, *Semiconductors—Basic Data* (Springer Verlag, Berlin, 1996) p. 317.
[36] T. Boykin, Phys. Rev. **B56**, 9613 (1997).
[37] M. Altarelli, U. Ekenberg, and A. Fasolino, Phys. Rev. **B32**, 5138 (1985).
[38] G. Klimeck, R. C. Bowen, and T. B. Boykin, IEEE Proc (2001) (accepted).
[39] C. Bowen, W. R. Frensley, and G. Klimeck, *IEEE Cornell Conference on Advanced Concepts in High Speed Semiconductor Devices and Circuits* (IEEE, New York, 1995) p. 435.
[40] T. S. Moise *et al.*, J. Appl. Phys. **78**, 6305 (1995).
[41] T. B. Boykin, Phys. Rev. **B51**, 4289 (1995).
[42] J. N. Schulman, Appl. Phys. Lett. **72**, 2829 (1998).
[43] G. Klimeck, R. C. Bowen, and T. B. Boykin, Phys. Rev. **B**, (2001) (accepted).
[44] R. K. Hayden *et al.*, Phys. Rev. **B49**, 10745 (1994).
[45] G. Klimeck *et al.*, Superlatt. Microstruct. **27**, 77 (2000).
[46] G. Klimeck, R. C. Bowen, T. B. Boykin, and T. A. Cwik, Superlatt. Microstruct. **27**, 519 (2000).

Appendix A. Dispersion bias dependence

Figure 8B shows the current density $J(k)$ as a function of bias. The streaks which correspond to high current densities resemble the transverse momentum dispersion if the voltage axis is scaled to energy by a factor of two. Section 6 shows through an analytic formula that the mapping of the transverse dispersion to the current density $J(k)$ is not exactly trivial. Current contributions are derived from a narrow energy range in the emitter ($\approx -8 \ldots 0$ meV) as the transverse dispersion is dragged through the Fermi sea with increasing bias. The resulting current density can be seen as a convolution of the dispersion in this energy range. To underline this point Fig. 19 shows the dispersions for three different bias points at 0.0, 0.2, and 0.4 V energy shifted by 0, 0.1, and 0.2 eV, respectively. One can observe that the spin splitting† increases as the bias is increased due to the increasing asymmetry in the Hamiltonian. The general shape of the dispersions remains the same. The strongest deviations can be seen for higher biases for the HH1 and HH2 states. This is attributed to the vanishing coupling to the emitter, the quantum well turning more into a triangular shape, and the collecor barrier being lowered. The imaginary bandwrapping from the conduction band to the valence band (see, for example, Fig. 7 in Ref. [7]) combined with the changing potential profile change the confinement significantly with applied bias. Such changes also have a profound influence on the resonance linewidth as discussed in Appendix B.

---

† The asymmetry of the applied bias has split the two spin states. Note that there is no magnetic field selection in these simulations. The spin degenerate states at $k = 0$ are split due to the translational symmetry breaking at $k > 0$. We use the notation $\uparrow$, $\downarrow$ as a shorthand to identify the two states. Since there is no selecting magnetic field we assume that, for example, LH1 $\uparrow$ consists of a linear combination of up and down spins.

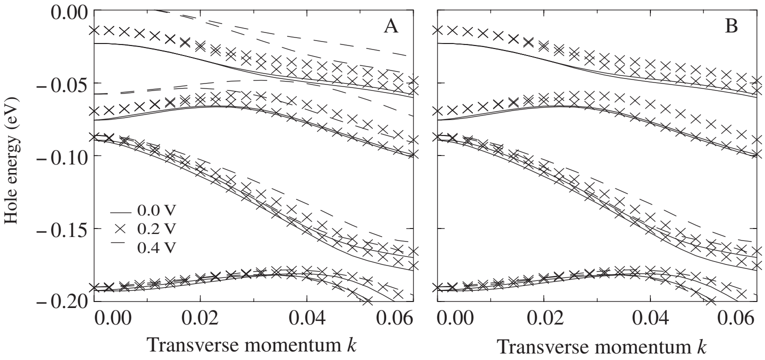

Fig. 19. Transverse subband dispersions for three different applied biases. 0.0, 0.2 and 0.4 V are depicted in solid lines, crosses, and dashed lines respectively. The energy scales are shifted by an energy corresponding to half the applied voltage. A, All the dispersion curves. B, same as A but, HH1 and HH2 for the 0.4 V dispersion eliminated. Spin splitting increases with increased bias, but general dispersion curve remains unchanged.

Appendix B. Resonance linewidths

Figure 20 sheds light on the interaction of HH and LH states and their coupling to the leads as a function of transverse momentum. Figure 20A shows the subband dispersion previously shown in Figs 2 and 5B in a smaller energy and transverse momentum range. Only the four top most states including the spins are depicted. From our analysis in Fig. 5 we can identify the two top most states as HH1. The shape of the dispersion of the two other states (in Fig. 20A) suggest that they should be associated with HH2 as discussed with Fig. 5 in Section 4.3. However, Fig. 2 in Section 4.2 identified the second state as LH1 by its nodal symmetry and resonance linewidth. Figure 20B shows the associated resonance linewidths as a function of transverse momentum of the first four states. The two highest states (HH1) show the expected narrow linewidths of about 10^{-8} eV at zero transverse momentum. However, the next two states have resonance and linewidths of about 5×10^{-4} eV which is indicative of the LH states. Figures 5 show an anticrossing of HH2 and LH1 at zero transverse momentum. This strong coupling results in the LH-like resonance width at zero transverse momentum. We therefore label the second states in Fig. 20A as HH2 + LH1.

Figure 20A also shows an anticrossing at a transverse momentum of about 0.022. This anticrossing has a very dramatic impact on the HH1 coupling to the leads as indicated by the large increase of the resonance linewidth by about three orders of magnitude compared to the zero transverse momentum result. This large increase in the resonance linewidth for this particular channel can result in a significant current increase as discussed in Fig. 12 in Section 6.6. This strong coupling will only have an impact if there is a significant number of carriers at the transverse momentum of 0.025. This is the case as the Fermi level or the temperature is increased as discussed in Section 7.

Appendix C. Material and sp3s* model parameters

The bandstructure and in particular the anisotropy of the hole bands in GaAs and AlAs has been studied extensively experimentally as well as theoretically [35]. Table 1 compares several band edges and effective masses from published data tables [35] to values computed using the sp3s* second-nearest neighbor tight-binding model with the parameters listed in Table 2.

The complete parameter list of the second-nearest neighbor model used in this publication is listed in Table 2. To achieve better fits to the experimental effective masses and bandgaps we have developed [45, 46] a genetic algorithm based procedure. The parameters used here have been optimized by Boykin [36] using analytical insights.

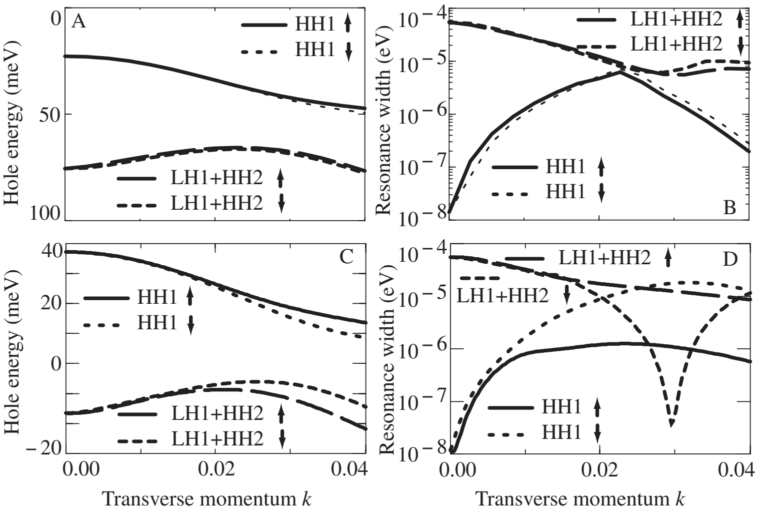

Fig. 20. A, Same hole dispersion shown in Fig. 5B in a smaller energy and momentum range. Only the four lowest energy hole states are shown including the spin. B, Resonance linewidth of the states in A. The HH1 states show a variation of the resonance linewidth of several orders of magnitude as a function of transverse momentum. The mixed state (LH1 + HH2) shows a reduction of resonance width by about an order of magnitude. The resonance interact very strongly at the anticrossing point $k = 0.022$. C, D, Same as A, B at a bias of 0.113 V. Increased asymmetry through bias increases the spin-splitting of the states and modifies the coupling to the leads strongly.

Table 1: Simulated effective masses and band edges for GaAs and AlAs based on the sp3s* second-nearest neighbor tight-binding model compared to experimental and theoretical data from Ref. [35].

	GaAs			AlAs		
Property	exp.	sim.	% dev	exp.	sim.	% dev
E_g^Γ	1.4240	1.4240	0.00	3.020	3.0217	0.06
Δ_{so}	0.3400	0.3664	7.76	0.300	0.3377	12.6
m_Γ^*	0.0670	0.0679	1.31	0.150	0.1574	4.95
$m_{lh}^*[001]$	−0.0871	−0.0708	18.7	−0.163	−0.1475	9.52
$m_{lh}^*[011]$	−0.0804	−0.0662	17.7	−0.140	−0.1259	10.1
$m_{lh}^*[111]$	−0.0786	−0.0649	17.5	−0.135	−0.1212	10.3
$m_{hh}^*[001]$	−0.4030	−0.4105	1.87	−0.516	−0.4782	7.33
$m_{hh}^*[011]$	−0.6600	−0.6929	4.99	−1.098	−1.0788	1.75
$m_{hh}^*[111]$	−0.8130	−0.8750	7.63	−1.570	−1.6206	3.22
m_{so}^*	−0.1500	−0.1440	3.98	−0.240	−0.2456	2.33

Table 2: Second-nearest neighbor tight-binding model parameters used in this paper for GaAs, AlAs, and Al$_{0.4}$GaAs. All parameters are in units of eV.

Parameter	GaAs	AlAs	Al$_{0.4}$GaAs
$E_{sa,sa}(000)$	−8.384281	−7.520109	−8.038610
$E_{pa,pa}(000)$	0.490469	0.341561	0.430906
$E_{sc,sc}(000)$	−2.758331	−1.797609	−2.374040
$E_{pc,pc}(000)$	3.670469	2.803311	3.323610
$E_{s^*a,s^*a}(000)$	8.590469	7.195801	8.032600
$E_{s^*c,s^*c}(000)$	6.720469	5.719251	6.319980
$V_{sa,sc}\left(\frac{1}{2}\frac{1}{2}\frac{1}{2}\right)$	−6.460530	−7.160000	−6.740320
$V_{xx}\left(\frac{1}{2}\frac{1}{2}\frac{1}{2}\right)$	2.260950	1.940000	2.132570
$V_{xy}\left(\frac{1}{2}\frac{1}{2}\frac{1}{2}\right)$	5.170000	4.500000	4.902000
$V_{sa,pc}\left(\frac{1}{2}\frac{1}{2}\frac{1}{2}\right)$	4.680000	5.072000	4.836800
$V_{sc,pa}\left(\frac{1}{2}\frac{1}{2}\frac{1}{2}\right)$	8.000000	8.000000	8.000000
$V_{s^*a,pc}\left(\frac{1}{2}\frac{1}{2}\frac{1}{2}\right)$	4.650000	3.280000	4.102000
$V_{pa,s^*c}\left(\frac{1}{2}\frac{1}{2}\frac{1}{2}\right)$	6.000000	1.750000	4.300000
$\lambda_{so,a}/3.0$	0.140000	0.140000	0.140000
$\lambda_{so,c}/3.0$	0.058000	0.008000	0.038000
$V_{sa,sa}(110)$	−0.010000	−0.010000	−0.010000
$V_{s^*a,s^*a}(110)$	0.000000	0.000000	0.000000
$V_{sa,s^*a}(110)$	0.000000	0.000000	0.000000
$V_{sa,xa}(110)$	0.050000	0.040000	0.046000
$V_{sa,xa}(011)$	0.058000	0.040000	0.050800
$V_{s^*a,xa}(110)$	0.020000	0.020000	0.020000
$V_{s^*a,xa}(011)$	0.040000	0.100000	0.064000
$V_{xa,xa}(110)$	0.320000	0.376900	0.342760
$V_{xa,xa}(011)$	−0.050000	−0.200000	−0.110000
$V_{xa,ya}(110)$	0.640000	1.200000	1.008000
$V_{xa,ya}(011)$	−1.000000	−1.200000	−1.080000
$V_{sc,sc}(110)$	−0.020000	−0.010000	−0.016000
$V_{s^*c,s^*c}(110)$	0.000000	0.000000	0.000000
$V_{sc,s^*c}(110)$	0.000000	0.000000	0.000000
$V_{sc,xc}(110)$	0.072000	0.073000	0.072400
$V_{sc,xc}(011)$	0.020000	0.040000	0.028000
$V_{s^*c,xc}(110)$	0.010000	0.030000	0.018000
$V_{s^*c,xc}(011)$	0.093500	0.030000	0.068100
$V_{xc,xc}(110)$	0.280000	0.495350	0.366140
$V_{xc,xc}(011)$	−0.100000	−0.166950	−0.126780
$V_{xc,yc}(110)$	0.200000	0.970000	0.708000
$V_{xc,yc}(011)$	−1.300000	−2.200000	−1.660000